

# MODULATION OF GALACTIC COSMIC RAYS IN THE INNER HELIOSPHERE OVER SOLAR CYCLES

Z.-N. SHEN<sup>1,2</sup> AND G. QIN<sup>3</sup>

<sup>1</sup>*State Key Laboratory of Space Weather, National Space Science Center, Chinese Academy of Sciences, Beijing 100190, China*

<sup>2</sup>*College of Earth Sciences, University of Chinese Academy of Sciences, Beijing 100049, China*

<sup>3</sup>*School of Science, Harbin Institute of Technology, Shenzhen, 518055, China; qingang@hit.edu.cn*

## ABSTRACT

The 11-year and 22-year modulation of galactic cosmic rays (GCRs) in the inner heliosphere are studied using a numerical model developed by Qin and Shen in 2017. Based on the numerical solutions of Parker's transport equations, the model incorporates a modified Parker heliospheric magnetic field, a locally static time delayed heliosphere, and a time-dependent diffusion coefficients model in which an analytical expression of the variation of magnetic turbulence magnitude throughout the inner heliosphere is applied. Furthermore, during solar maximum, the solar magnetic polarity is determined randomly with the possibility of  $A > 0$  decided by the percentage of the north solar polar magnetic field being outward and the south solar polar magnetic field being inward. The computed results are compared with several GCR observations, e.g., IMP 8, SOHO/EPHIN, Ulysses, Voyager 1 & 2, at various energies and show good agreement. It is shown that our model has successfully reproduced the 11-year and 22-year modulation cycles.

*Keywords:* cosmic rays - diffusion - Sun: activity - turbulence - Sun: heliosphere

## 1. INTRODUCTION

Galactic cosmic rays (GCRs) are modulated by interplanetary magnetic field (IMF) while transporting inside the heliosphere, and show a  $\sim 11$ -year cycle variation (e.g., McDonald 1998; Shen & Qin 2016). Furthermore, one observes a  $\sim 22$ -year cycle of the intensities of GCRs with peak-like or plateau-like temporal profiles in solar minimum during negative or positive solar magnetic polarity, respectively. Theoretical and numerical models have successfully illustrated that the variation of GCRs in the heliosphere is caused by the modulation processes, including convection, diffusion, drifts, and adiabatic energy changes (see, e.g., Parker 1965; Zhang 1999; Pei et al. 2010b; Strauss et al. 2012; Potgieter 2013; Zhao et al. 2014; Qin & Shen 2017).

The temporal profiles of GCRs also show some short-term variations, including the  $\sim 27$ -day solar rotation variations and irregular variations such as Forbush decreases (Cane 2000; Richardson 2004; Alania et al. 2011; Shen & Qin 2016). The  $\sim 27$ -day variations of GCRs are caused by the passage of corotating interaction regions (CIRs, Richardson 2004). The GCR depressions onset is thought to be related to the stream interfaces and the leading edges of CIRs (Richardson et al. 1996), and diffusion has a more important role than drifts in  $\sim 27$ -day modulation of GCRs (Guo & Florinski 2016). In addition, the  $\sim 27$ -day variation amplitudes of GCR during  $A > 0$  (magnetic field in the northern hemisphere directed outward the Sun) solar minima are larger than that during  $A < 0$  (magnetic field in the northern hemisphere directed toward the Sun) solar minima (Richardson et al. 1999; Alania et al. 2001; Kota & Jokipii 2001). Gil & Mursula (2017) summarized that for the  $\sim 27$ -day modulation of GCRs, the heliospheric current sheet (HCS) plays an important role during  $A < 0$  solar minima, and the latitude dependent solar wind velocity is more important during  $A > 0$  solar minima. Forbush decreases (FDs) are short-term decreases in GCR intensity followed by a substantially slower recovery (Lockwood 1971; Cane 2000). They are typically caused by the interplanetary counterparts of coronal mass ejections (CMEs) from the Sun. Cane (2000) depicted a classical two-step FD, where the first step of the decrease is caused by the turbulent field generated behind the CME associated interplanetary shock and the second step is caused by the closed field line geometry of CME ejecta. Wawrzynczak & Alania (2010) studied the temporal variabilities of the rigidity spectrum exponent of FD, and showed that the hardening rigidity spectrum was

caused by the increased magnetic turbulence. Utilizing the measurements from the worldwide neutron monitor stations, [Zhao & Zhang \(2016\)](#) studied two prominent FD events during solar cycle 24 with comparable decrease magnitudes but distinctly different evolution of GCR energy spectrum and the energy dependence of recovery time. The different solar wind structures were thought to account for the difference ([Zhao & Zhang 2016](#)). While propagating outward, the corotating streams or CME generated transient solar wind flows usually merge to form various types of large interaction regions, e.g., the merged interaction regions (MIRs, [Burlaga et al. 1993](#); [Cane 2000](#)) with the largest ones known as global MIRs (GMIRs). The GMIRs, which are considered to be related to CMEs ([Cane 2000](#)), can cause large decrease in GCR intensity and are treated as propagating diffusion barriers in some modeling works (e.g., [Potgieter & Le Roux 1992](#); [Le Roux & Potgieter 1995](#)). During the 11-year solar cycle, barrier modulation is dominant at solar maximum, and drift effects are thought to control modulation during solar minimum ([Cliver et al. 2013](#); [Potgieter 2013](#)). Note that CIRs do not contribute to the 11-year modulation cycle ([Potgieter 2013](#)), while a series of GMIRs may be responsible for the long-term GCR modulation during the increasing phase of solar activity ([Potgieter & Le Roux 1992](#); [Le Roux & Potgieter 1995](#)).

Modulation in steady-state has been well studied by previous works ([Potgieter 2013](#); [Potgieter et al. 2014](#); [Zhao et al. 2014](#)). [Potgieter et al. \(2014\)](#) studied the modulation of proton spectra with the PAMELA data from July 2006 to 2009, and they concluded that the recent solar minimum was “diffusion dominated”. In the work of [Potgieter et al. \(2014\)](#), parameters in diffusion coefficients and drifts coefficients were adapted to observations (see also [Potgieter et al. 2015](#); [Raath et al. 2016](#)). [Zhao et al. \(2014\)](#) studied modulation of GCRs energy spectra during the past three solar minima using an empirical diffusion coefficient model according to [Zhang \(1999\)](#). They found that decreased perpendicular diffusion in polar direction, which is in contrast to the assumption of enhanced diffusion in polar regions that was used to explain the observed Ulysses CR gradients (see, e.g., [Potgieter 2000](#)), and increased parallel diffusion might be the reason for the record high-level of GCR intensity measured at Earth. Since the diffusion coefficients describe the scattering of GCRs by random fluctuations in the IMF, turbulence quantities are needed in the diffusion theory. In solar wind, the evaluation of turbulence are well described by magnetohydrodynamic (MHD) theory ([Marsch & Tu 1989](#); [Zhou & Matthaeus 1990](#)), and the turbulence transport throughout the

heliosphere has been studied over the years (e.g., Zank & Matthaeus 1993; Zank et al. 1996, 2012, 2017; Matthaeus et al. 1999; Smith et al. 2001; Breech et al. 2008; Hunana & Zank 2010; Oughton et al. 2011; Wiengarten et al. 2016). With the turbulence transport models, the diffusion tensor is able to be calculated, (e.g., Zank et al. 1998; Pei et al. 2010a; Engelbrecht & Burger 2013; Zhao et al. 2017). Theoretical and numerical works have shown that drift coefficients can be reduced in the presence of turbulence, (e.g., Jokipii 1993; Fisk & Schwadron 1995; Giacalone & Jokipii 1999; Candia & Roulet 2004; Stawicki 2005; Minnie et al. 2007; Tautz & Shalchi 2012), see also the first-order approach in Engelbrecht et al. (2017). The reduced drift coefficients, which are obtained from fitting the simulation results (Burger & Visser 2010; Tautz & Shalchi 2012), are also used together with the turbulence transport theory to study the modulation of GCRs (e.g., Engelbrecht & Burger 2013). Using the Nearly Incompressible (NI) MHD turbulence transport model developed by Zank et al. (2017), Zhao et al. (2017) also showed the effect of both weak and moderately strong turbulence on drift coefficients. Since there exists close coupling between turbulence, solar wind, and energetic particles, some work combine large-scale solar wind flow with small-scale fluctuations in a self-consistent way (see, e.g., Usmanov et al. 2011, 2014, 2016; Wiengarten et al. 2015; Shiota et al. 2017) to study the spatial variations of the diffusion coefficients (see, e.g., Chhiber et al. 2017). Furthermore, using a diffusion coefficient model according to Giacalone & Jokipii (1999), Guo & Florinski (2016) studied the modulation of GCRs by CIRs at 1 au. They combined the small-scale turbulence transport with the MHD background for the simulation of cosmic-ray transport to show short-term modulation effects.

In order to describe the cosmic-ray modulation over long periods, time-dependent modulation processes are needed. Perko & Fisk (1983) used a one-dimensional numerical model to study the time-dependent modulation of GCRs for the first time. Le Roux & Potgieter (1990) established a time-dependent two-dimensional numerical model, which incorporated a time-dependent drift model and the wavy HCS varying with time and propagating outward at the solar wind speed. Observations show that large cosmic-ray transient decreases are caused by MIRs and GMIRs (Burlaga et al. 1993; Webber & Lockwood 1993). Therefore, some time-dependent modulation models used the combination of drifts and GMIRs (e.g., Potgieter et al. 1993; Le Roux & Potgieter 1995) to provide a complete 22-year modulation cycle.

Ferreira & Potgieter (2004) used a two-dimensional numerical model, and suggested a compound approach, which combined the effects of the changes in the HMF magnitude with drifts, also time-dependent current-sheet tilt angles. Thus, they established a time dependence in the diffusion and drift coefficients. This approach adopted the concept of propagating diffusion barriers (see, e.g., Burlaga et al. 1993; Le Roux & Potgieter 1995), and gave lower values of diffusion coefficients and drifts for solar maximum than for solar minimum. Using the model established by Ferreira & Potgieter (2004), Ndiitwani et al. (2005) studied modulation of GCRs along the trajectory of Ulysses and concluded that drifts needed an additional decrease during solar maximum. Based on their works, Manuel et al. (2011b) and Manuel et al. (2014) considered the dependence of diffusion coefficients on turbulence nature (e.g., Teufel & Schlickeiser 2002, 2003; Shalchi et al. 2004; Minnie et al. 2007) and developed an improved compound approach. Such compound approaches were incorporated in numerical modulation model, and the computed results agreed well with observations at various energies. Bobik et al. (2012) established a 2D heliospheric modulation (HelMod) model with a re-scaled heliosphere which was divided into radially equally-spaced slices. In their work, the time-dependent modulation parameter  $K_0$  in diffusion coefficients was determined by the modulation strength which was given by the force-field model (FFM, see, e.g., Gleeson & Axford 1968; Gleeson & Urch 1971). Then they fitted  $K_0$  with the sunspot numbers and the neutron monitor counting rates for periods of low and high solar activities, respectively. Boschini et al. (2017a) used this model to study modulation of GCRs with energy approximately larger than 0.5 GeV/nucleon, and the numerical results were consistent with the observations of PAMELA, AMS-02 and Ulysses. Qin & Shen (2017) used a new diffusion coefficients model NLGCE-F from Qin & Zhang (2014) to study the modulation of GCRs from 2006 to 2009. The NLGCE-F model was obtained by fitting the numerical solutions of nonlinear perpendicular (NLGC, Matthaeus et al. 2003) and parallel (NLPA, Qin 2007) diffusion theories with polynomials, so it can help us calculate the diffusion coefficients directly without the iteration solution of integration equations set. The NLGCE-F model needs turbulence quantity throughout the heliosphere, which has been studied by turbulence transport models (see, e.g., Zank et al. 1996, 2012, 2017; Breech et al. 2008; Pei et al. 2010a; Oughton et al. 2011; Engelbrecht & Burger 2013). However, Qin & Shen (2017) only considered the variability of magnetic turbulence magnitude in the heliosphere for simplicity. They established an an-

alytical expression, denoted as TRST, to describe the spatial variability of turbulence magnitude, which is consistent with the Ulysses, Voyager 1 & 2 observations. The turbulence model TRST was then inserted into the diffusion model NLGCE-F to establish a time and space dependence in the diffusion coefficients.

The main purpose of this paper is to reproduce the  $\sim 11$ - and  $\sim 22$ -year solar cycle variation of GCRs using the numerical modulation model based on [Qin & Shen \(2017\)](#). In section 2, we show interplanetary conditions observed near Earth and briefly discuss the HMF polarity in solar maximum. In section 3, we discuss the GCR modulation model, including particle drifts and diffusion coefficients. Computation results are compared with observations of IMP 8, Ulysses, Voyager 1 & 2 at various energies in section 4. Conclusions and discussion are presented in section 5.

## 2. INTERPLANETARY CONDITIONS IN THE INNER HELIOSPHERE

Solar activities show 11-year cycles, heliospheric parameters embedded in the solar wind plasma also show cyclic variabilities related to solar cycles. In our model, several time-varying heliospheric parameters are needed to study the long-term modulation of GCRs. Figure 1 illustrates observations of interplanetary conditions as a function of time for the period 1976-2016. Top panel shows the computed tilt angle  $\alpha$  for the new model from Wilcox Solar Observatory ([wso.stanford.edu](http://wso.stanford.edu)). HCS is nearly flat during solar minimum and the maximum values of tilt angle reach above  $70^\circ$  around solar maximum. Second and third panels are monthly averaged solar wind speed and HMF strength near Earth using data from OMNI website ([omniweb.gsfc.nasa.gov](http://omniweb.gsfc.nasa.gov)). The solar wind speed does not show a clear 11-year cycle, while the HMF strength depicts an 11-year cycle. It is noted that in 2009 the HMF reached the lowest value of about 3 nT since 1963. The last panel means the square root of magnetic field variances (magnetic turbulence magnitude) calculated using the method described in [Qin & Shen \(2017\)](#), and minutely HMF data from OMNI website is used to get more accurate result. Note that solar wind data in months of November 1982, December 1982 and January 1983 are not available, we use the linear interpolation method to get the monthly values of solar wind velocity.

In addition, HMF changes its dipole polarity during solar maximum and resulting in a 22-year magnetic cycle. In Figure 2, top panel means the sunspot number from the World Data Center SILSO (WDC-SILSO, [sidc.be/silso/](http://sidc.be/silso/)), the second panel represents the north (black solid line) and south (red dotted line) polar

magnetic field strength, and the positive (negative) value of north solar polar field indicates HMF points outward (inward) in the northern hemisphere of the Sun, which is also noted as the  $A > (A < 0)$  polarity cycle. Hereafter we denote the north and south solar polar field strength as  $B_N$  and  $B_S$ , respectively. The solar polar magnetic field reverses its polarity every  $\sim 11$  years and this causes the charge-sign dependent modulation and a 22-year solar modulation of GCRs. Therefore, the solar magnetic polarity plays an important role in the cosmic ray modulation theory. However, during solar maximum, it is difficult to identify the Sun's magnetic polarity, which is assumed as random. For any time interval of one month, we calculate the percentage  $P_A$  of positive value in data set  $B_N$  and  $-B_S$ , which is shown in the bottom panel of Figure 2. We assume the possibility of  $A > 0$  in this month is  $P_A$ . From the bottom panel of Figure 2 we can see that  $P_A$  varies in the range of  $[0, 1]$  around solar maximum, while  $P_A = 1$  or  $P_A = 0$  during the period away from solar maximum.

### 3. MODULATION MODEL AND NUMERICAL METHODS

Galactic cosmic rays are modulated by solar activities while transporting in the heliosphere, and the modulation processes are governed by the well known Parker transport equation (TPE) (Parker 1965),

$$\frac{\partial f}{\partial t} = -(\mathbf{V}_{sw} + \langle \mathbf{v}_d \rangle) \cdot \nabla f + \nabla \cdot (\mathbf{K}_s \cdot \nabla f) + \frac{1}{3} (\nabla \cdot \mathbf{V}_{sw}) \frac{\partial f}{\partial \ln p}, \quad (1)$$

where  $f(\mathbf{r}, p, t)$  is the omnidirectional cosmic-ray distribution function, with  $\mathbf{r}$  the spatial position in a heliocentric spherical coordinate system,  $p$  the particle momentum,  $t$  the time. The cosmic-ray intensity  $j = p^2 f$ .  $\mathbf{V}_{sw}$  is the solar wind velocity,  $\langle \mathbf{v}_d \rangle$  is the pitch-angle averaged drift velocity, and  $\mathbf{K}_s$  is the symmetric part of diffusion tensor, which has three components in the field-aligned conditions, a parallel diffusion coefficient  $\kappa_{\parallel}$  and two perpendicular diffusion coefficients, in the radial direction ( $\kappa_{\perp r}$ ) and the polar direction ( $\kappa_{\perp \theta}$ ). In this work, we assume the solar wind velocity is radial and the magnitude remains constant in the inner heliosphere. Thus  $(\nabla \cdot \mathbf{V}_{sw}) > 0$  and the last term on the right hand side represents adiabatic energy losses.

The background HMF, which is embedded in the solar wind plasma, is usually assumed to have an Archimedean spiral due to the solar rotation (Parker 1958). However, the standard Parker HMF is always modified over the polar regions of the heliosphere to scale down the excessive drift effects (Potgieter et al.

1989; Potgieter 2013; Raath et al. 2016; Qin & Shen 2017). HMF observations at high latitude also show significant deviations from what the standard Parker model predicts (Forsyth et al. 1996). Thus several modifications of Parker HMF has been proposed, Jokipii & Kota (1989) introduced a small latitudinal component, Smith & Bieber (1991) added an additional azimuthal term, Fisk (1996) included the footprint motion of HMF field lines to account for observations of recurrent energetic particle events and smaller cosmic ray intensities at higher latitudes (see, e.g., Simpson et al. 1996; Zhang 1997). However, the Fisk type HMF is difficult to handle to some extent, and its existence is also debated (e.g., Zurbuchen et al. 1997; Roberts et al. 2007; Sternal et al. 2011), see the review in Potgieter (2017). Following Qin & Shen (2017), we use the modification proposed by Jokipii & Kota (1989) in this work, and the modified expression can be written as (Langner 2004)

$$\mathbf{B} = \frac{AB_0}{r^2} \left( \mathbf{e}_r + \frac{r\delta(\theta)}{r_s} \mathbf{e}_\theta - \frac{(r-r_s)\Omega \sin \theta}{V_{sw}} \mathbf{e}_\phi \right) [1 - 2H(\theta - \theta')], \quad (2)$$

where  $\mathbf{e}_r$ ,  $\mathbf{e}_\theta$ , and  $\mathbf{e}_\phi$  are unit vectors in the radial, latitudinal, and azimuthal directions, respectively;  $B_0$  is a constant that allows  $|\mathbf{B}|$  equal to the HMF magnitude value at Earth;  $A = 1$  ( $A = -1$ ) describes the  $A > 0$  ( $A < 0$ ) solar cycle and the HMF points outward (inward) in the northern hemisphere of Sun;  $\delta(\theta)$  is the perturbation parameter,  $r_s$  is the radius of the source surface where the HMF is assumed to point radially outward,  $\Omega = 2.66 \times 10^{-6}$  rad s $^{-1}$  is the angular speed of Sun's rotation,  $H$  is the Heaviside function,  $\theta'$  is the HCS latitudinal extent whose expression is given by Kota & Jokipii (1983),

$$\theta' = \frac{\pi}{2} - \arctan \left[ \tan \alpha \sin \left( \phi + \frac{(r-r_s)\Omega}{V_{sw}} \right) \right]. \quad (3)$$

According to Langner (2004), we can express the perturbation parameter as

$$\delta(\theta) = \frac{\delta_m}{\sin \theta} \quad (4)$$

to obtain  $\nabla \cdot \mathbf{B} = 0$ . In order to avoid singularity, we use a reflective boundary condition near the poles,  $\theta = 2\theta_0 - \theta$ , for  $\theta < \theta_0$  if  $\theta < 90^\circ$  or  $\theta > \theta_0$  if  $\theta > 90^\circ$ . In the work of Jokipii & Kota (1989), the value of  $\delta(\theta)$  was suggested in the range of  $10^{-3} - 3 \times 10^{-3}$ . Bobik et al. (2013) also studied the value of  $\delta_m$ , and  $2 \times 10^{-5}$  was selected to compare with the observations in cycle 23. Thus  $\delta_m$  may be different in each solar cycle. However, the variation of  $\delta_m$  within the range suggested by Bobik et al. (2013) does not

have much modulation effect in our model (see also, [Boschini et al. 2017a](#)). Therefore, in this study we set  $\delta_m = 2 \times 10^{-5}$  ([Bobik et al. 2013](#); [Boschini et al. 2017a](#)),  $\theta_0 = 2.5^\circ$  if  $\theta < 90^\circ$  and  $\theta_0 = 177.5^\circ$  if  $\theta > 90^\circ$ . It is shown that this modification can significantly enhance the magnetic field intensity and reduce the drift velocity at large radial distance in polar regions of the heliosphere without influence the equatorial regions obviously ([Bobik et al. 2012, 2013](#); [Qin & Shen 2017](#)).

According to [Sheeley et al. \(1997\)](#), the solar wind speed accelerates from zero to a constant within 0.3 au from the Sun. During solar minimum, observations have shown that solar wind speed increases from  $\sim 400 \text{ km s}^{-1}$  in the equatorial plane to  $\sim 800 \text{ km s}^{-1}$  in high latitudes ([McComas et al. 2002](#); [Zurbuchen 2007](#)). However, such simple pattern does not exist anymore during solar maximum ([Heber & Potgieter 2006](#)). Some works use a hyperbolic function to present such variability during solar minimum, and the function can be expressed as (see, e.g., [Hattingh 1998](#); [Heber & Potgieter 2006](#); [Potgieter 2013](#))

$$\mathbf{V}_{sw}(r, \theta) = V_{model} \mathbf{e}_r = V_0 \left\{ 1 - \exp \left[ \frac{40}{3} \left( \frac{r_s - r}{r_0} \right) \right] \right\} \left\{ 1.475 \mp 0.4 \tanh \left[ 6.8 \left( \theta - \frac{\pi}{2} \pm \xi \right) \right] \right\} \mathbf{e}_r, \quad (5)$$

with  $V_0 = 400 \text{ km/s}$ ,  $r_0 = 1 \text{ au}$  and  $\xi = \alpha + 15\pi/180$ . The top and bottom sign correspond to the northern and southern hemisphere, respectively. Note that coefficients in Equation (5) are obtained by comparing with the observations of Ulysses (see, e.g., [Hattingh 1998](#)). [Potgieter et al. \(2013\)](#) classified the solar activity in terms of  $\alpha$ , with  $\alpha \leq 30^\circ$ ,  $30^\circ < \alpha \leq 60^\circ$  and  $60^\circ < \alpha \leq 90^\circ$  represents periods of low, moderate and high solar activities respectively. In this work, we assume the solar wind speed has no latitudinal variation during periods of moderate and high solar activities with value  $V_{1au}$  extracted from OMNI data set (see, e.g., [Bobik et al. 2012](#)). Thus the solar wind speed model used in this work can be expressed as follows,

$$V_{sw} = \begin{cases} V_{model}, & \text{for } \alpha \leq 30^\circ \\ V_{1au}, & \text{for } \alpha > 30^\circ. \end{cases} \quad (6)$$

Figure 3 (left) shows the result of Equation (6) along the trajectory of Pioneer 11. The radial distance (black line) and heliographic latitude (red line) of Pioneer 11 are illustrated in the top panel. Black and red lines in the bottom panel indicate daily solar wind speed observed by Pioneer 11 and monthly solar wind speed predicted by Equation (6), respectively, along the trajectory of Pioneer 11. It is shown that

Equation (6) can show the trend of solar wind speed in the latitude dependence comparing with Pioneer 11 observations during solar minimum. We also show the daily solar wind speed observations of Ulysses (black line) and the result of Equation (6) along the trajectory of Ulysses (red line) in the bottom panel of Figure 3 (right). The characteristics of solar wind velocity during solar maximum and minimum can be seen clearly. Better agreement between the Ulysses observation and Equation (6) is obtained because the coefficients in Equation (6) are got by comparing with Ulysses observations (e.g., [Hattingh 1998](#)). Note that for simplicity, while solving the TPE Equation (1) numerically in each step we assume the magnitude of solar wind as a constant with the value calculated with Equation (6).

The drift coefficient can be suppressed by magnetic turbulence in solar wind plasma (see, e.g., [Jokipii 1993](#); [Fisk & Schwadron 1995](#); [Giacalone & Jokipii 1999](#); [Candia & Roulet 2004](#); [Stawicki 2005](#); [Minnie et al. 2007](#); [Tautz & Shalchi 2012](#)). However, it is complicated to use the reduction of drift effects self-consistently (see, e.g., [Bieber & Matthaeus 1997](#); [Burger & Visser 2010](#); [Tautz & Shalchi 2012](#)) or in Ad hoc form (see, e.g., [Burger et al. 2000](#); [Potgieter 2013](#); [Vos & Potgieter 2016](#); [Nndanganeni & Potgieter 2016](#)) in modulation works. The effects of turbulence on GCR drifts are far from complete to be understood. Therefore, we use the weak scattering drift coefficient for simplicity in this work. The general weak-scattering drift velocity can be written as ([Jokipii et al. 1977](#))

$$\langle \mathbf{v}_d \rangle = q \frac{P\beta}{3} \nabla \times \left( \frac{\mathbf{B}}{B^2} \right), \quad (7)$$

with  $q$  the particle charge sign,  $P$  the rigidity of particle,  $\beta$  the ratio between the speed of particle  $v$  and that of light, and  $B$  the magnitude of modified Parker HMF. The drift velocity is usually divided into two components ([Burger & Potgieter 1989](#)), i.e., the combination of gradient and curvature drifts  $\mathbf{v}_{gc}$  which are caused by the large scale HMF, and the current sheet drift  $\mathbf{v}_{ns}$  when particles across or transport near the HCS. Gradient and curvature drifts could lead to a  $\sim 22$ -year cycle of GCR intensity and the charge-sign dependent modulation ([Jokipii et al. 1977](#)). Positively charged GCRs mainly drift inward from polar regions during  $A > 0$  polarity solar cycles, and mainly drift inward along the HCS in equatorial regions during  $A < 0$  polarity solar cycles. Thus drifts will produce flat and sharp temporal profiles of positively charged GCR intensity during the  $A > 0$  and  $A < 0$  solar minima, respectively. This effect reverses for negatively charged

GCRs. The detailed description and derivation of drifts for the modified Parker HMF Equation (2) can be found in Qin & Shen (2017).

Magnetic turbulence in solar wind plasma causes diffusion of cosmic rays parallel and perpendicular to the background HMF. Scattering theories have been developed to describe the properties of the diffusion coefficients (see e.g., Jokipii 1966; Matthaeus et al. 2003; Qin 2007; Qin & Zhang 2014). Following Qin & Shen (2017), we use the NLGCE-F model which is in the polynomial form by fitting the numerical results from simultaneously solving nonlinear theories of parallel and perpendicular diffusion (Qin 2007; Qin & Zhang 2014). The expressions of the NLGCE-F model are as follows,

$$\ln \frac{\lambda_\sigma}{\lambda_{slab}} = \sum_{i=0}^{n_{\sigma 1}} a_i^\sigma \left( \ln \frac{R_L}{\lambda_{slab}} \right)^i \quad (8)$$

with

$$a_i^\sigma = \sum_{j=0}^{n_{\sigma 2}} b_{i,j}^\sigma \left( \ln \frac{E_{slab}}{E_{total}} \right)^j \quad (9)$$

$$b_{i,j}^\sigma = \sum_{k=0}^{n_{\sigma 3}} c_{i,j,k}^\sigma \left( \ln \frac{\delta B^2}{B^2} \right)^k \quad (10)$$

$$c_{i,j,k}^\sigma = \sum_{l=0}^{n_{\sigma 4}} d_{i,j,k,l}^\sigma \left( \ln \frac{\lambda_{slab}}{\lambda_{2D}} \right)^l, \quad (11)$$

where  $\sigma$  means  $\perp$  or  $\parallel$ , diffusion coefficients  $\kappa_\sigma = \frac{\lambda_{\sigma v}}{3}$  and we assume  $\kappa_{\perp r} = \kappa_{\perp \theta}$  in this work,  $\lambda_{slab}$  is the spectral bend-over scale of the slab component of turbulence and  $\lambda_{2D}$  is that of the 2D component,  $E_{slab} = \langle \delta B^2_{slab} \rangle$  means the magnetic turbulence energy in the slab component and  $E_{total} = \langle \delta B^2 \rangle$  is the total magnetic turbulence energy,  $R_L$  means the particle's gyro-radius, and  $\delta B/B$  represents the turbulence level. The polynomial order  $n_{\sigma i}$  and coefficients  $d_{i,j,k,l}^\sigma$  in Equation (8) are obtained from Qin & Zhang (2014), and the computer code for the NLGCE-F diffusion coefficients model can be found on the website at <http://www.qingang.org.cn/code/NLGCE-F>. According to Qin & Zhang (2014), input parameters should vary within specified ranges, shown as follows, to ensure the validity of NLGCE-F model,

$$1 \lesssim \frac{\lambda_{slab}}{\lambda_{2D}} \lesssim 10^3, \quad (12)$$

$$10^{-3} \lesssim \frac{E_{slab}}{E_{total}} \lesssim 0.85, \quad (13)$$

$$10^{-4} \lesssim \frac{\delta B^2}{B^2} \lesssim 10^2, \quad (14)$$

$$10^{-5} \lesssim \frac{R_L}{\lambda_{slab}} \lesssim 6.3. \quad (15)$$

Note that, to insure the values of input parameters in Equation (8) vary within valid ranges, the particle's energy should be not much more than 10 GeV and the modulation boundary of the numerical model should be set inside the termination shock (TS) (Qin & Shen 2017).

Characteristics of HMF and turbulence in solar wind plasma throughout the heliosphere are needed to calculate diffusion coefficients with the NLGCE-F model. Considering two-component model of turbulence (Matthaeus et al. 1990a) in solar wind, turbulence quantities have been studied by turbulence transport models (TTMs) (Zank et al. 1996, 2012, 2017; Breech et al. 2008; Pei et al. 2010a; Oughton et al. 2011; Engelbrecht & Burger 2013). To some extent, it is complicated to apply the TTMs in long-term modulation of GCRs. In addition, the turbulence parameters in solar wind, such as  $\lambda_{slab}$  and  $\lambda_{2D}$ , can not be observed by spacecraft directly and should be studied with some theoretical work, so their detailed knowledge is not complete (e.g., Matthaeus et al. 1990a; Adhikari et al. 2017). Therefore, we set them in simple forms according to some study for solar wind near Earth. Observational studies (Osman & Horbury 2007; Dosch et al. 2013) have indicated that  $\lambda_{slab}$  is about a factor of two larger than  $\lambda_{2D}$ . According to new results from multi-spacecraft measurements (Weygand et al. 2009, 2011), for the slow solar wind, the correlation scale ratio of slab to 2D is around 2.6 while in the fast wind the ratio is around 0.7. Observations found that the ratio of the 2D and slab turbulence energy is about 80%:20% (Matthaeus et al. 1990b; Bieber et al. 1994), and the ratio can be different in slow and fast solar wind (Dasso et al. 2005). In solar wind and solar corona, the plasma beta ( $\beta_p$ ) is of the order of  $\beta_p \sim 1$  and  $\beta_p \ll 1$ , and the 2D and slab energy ratio 80%:20% is usually used in some theoretical work based on this assumption (Zank & Matthaeus 1992, 1993; Hunana & Zank 2010). In addition, the correlation scales and energies of 2D and slab turbulence may also vary with solar cycles, but it still needs some further study. Therefore, in this work, we set  $\lambda_{slab}/\lambda_{2D} = 2.6$ ,  $\lambda_{slab} = 0.02r$  (Qin & Shen 2017),  $E_{slab}/E_{total} = 0.2$ , and only consider the spatial and temporal changes of magnetic turbulence magnitude  $\delta B$  in the heliosphere for simplicity.

Note that, NLGC has also been derived into many analytical expressions, e.g., Zank et al. (2004) and Shalchi et al. (2004), which are used in many simulation models with the parallel diffusion coefficient from

the quasilinear theory (QLT, Jokipii 1966) as input. However, QLT is not very accurate compared to the simulation results because of the nonlinear effect (e.g., Qin et al. 2002). Based on the NLGC theory, Qin (2007) combined the nonlinear theory of parallel and perpendicular diffusion together to obtain the NLGC-E model, which is shown to agree better with simulation results than original NLGC with parallel diffusion from QLT as input. Besides, NLGCE-F also solves the case that NLGC fails in pure slab or pure 2D turbulence.

For the radial dependence of  $\delta B$ , some studies use analytical expressions to approximate the solutions of TTMs (see, e.g., Zank et al. 1996; Burger et al. 2008; Effenberger et al. 2012; Ngobeni & Potgieter 2014; Strauss et al. 2017), and the latitudinal dependence of  $\delta B$  can be inferred from the magnetic field observations of Ulysses (Perri & Balogh 2010). Based on those studies, Qin & Shen (2017) utilized an analytical expression, denoted as TRST, to describe the spatial variations of  $\delta B$  as follows,

$$\delta B = \delta B_{1\text{au}} R^S \left( \frac{1 + \sin^2 \theta}{2} \right), \quad (16)$$

where  $\delta B_{1\text{au}}$  means the magnetic turbulence magnitude near Earth,  $R = r/r_0$  with  $r_0 = 1$  au, and  $S$  varies as a function of the HCS tilt angle  $\alpha$  according to Qin & Shen (2017),

$$S = -1.56 + 0.09 \ln \frac{\alpha}{\alpha_c}, \quad (17)$$

where  $\alpha_c = 1^\circ$ . Figure 4 shows  $S$  varies with time. It is clearly shown that  $S$  has an 11-year cycle.  $\delta B$  decreases as  $\sim r^{-1.19}$  and  $\sim r^{-1.4}$  during solar maximum and solar minimum, respectively. We can infer from the prediction of WKB theory that  $\delta B$  decays as  $r^{-1.5}$ . In the interplanetary space, stream shear, shock wave and pickup ions can be sources of turbulence (Zank et al. 1996; Smith et al. 2001). Zank et al. (1996) pointed out that the dissipation rate of turbulence energy is proportional to the source of turbulence. Adhikari et al. (2014) also verified that the temporally varying sources of turbulence depend on heliocentric distance, and all sources should be considered to fit the observations well. Considering all sources of turbulence, theoretical works (see, e.g., Zank et al. 1996; Smith et al. 2001; Adhikari et al. 2014) have shown that the dissipation rate of turbulence energy is slower than that predicted by WKB theory. The parameters in TRST model are chosen to fit the spacecraft observations, and the complicated processes considered by TTMs have not been studied in this work. However, the dissipation rate of turbulence energy given by the

TRST model is also slower than that predicted by WKB theory. It has been shown by [Qin & Shen \(2017\)](#) that the TRST model agrees well with the magnetic turbulence magnitude observed by Ulysses, Voyager 1 and Voyager 2 measurements.

We are able to compute diffusion coefficients at any time and location using diffusion coefficients model Equation (8) with the modified Parker HMF Equation (2) and the TRST model. The input parameters, i.e., HMF strength at 1 au,  $\delta B_{1\text{au}}$ , and HCS tilt angle  $\alpha$  can be obtained from observations near Earth. This diffusion coefficients model has been tested by reproducing the time-varying proton spectra observed by PAMELA during the past solar minimum ([Qin & Shen 2017](#)). In this work, we would continue to test it with GCR flux observed by various spacecraft, e.g., Ulysses, Voyager 1, &2, over solar cycles. As an example, we show the computed monthly parallel and perpendicular mean-free paths as well as the particle's gyro-radius, which is equivalent to the particle's drift scale with the assumption of weak scattering, for 1 GV proton near Earth in the top, middle and bottom panel of Figure 5, respectively. As the original results have shown too many spikes, we present the 13-month smoothed values in this figure. The  $\sim 11$ -year variation cycles are identifiable in the temporal profiles of  $\lambda_{\parallel}$  and  $R_L$ , both of which reach quite low levels around solar maxima. The drift scale, as the turbulence effect not considered, is proportional to  $B^{-1}$  and anti-correlated with solar activity. The profile of  $\lambda_{\perp}$  presents some different variabilities, and there is no clear relationship between  $\lambda_{\parallel}$  and  $\lambda_{\perp}$ . However, in the recent solar minimum, both  $\lambda_{\parallel}$  and  $\lambda_{\perp}$  show a large increase. The variations of turbulence magnitude  $\delta B$  and IMF magnitude  $B$  can cause the solar cycle variations of  $\lambda_{\parallel}$  and  $\lambda_{\perp}$ . For a fixed  $B$ , the decreased  $\delta B$  can result in an increase in  $\lambda_{\parallel}$  and a decrease in  $\lambda_{\perp}$ . On the other hand, for a fixed  $\delta B$ , the decreased  $B$  can result in a decrease in  $\lambda_{\parallel}$  and an increase in  $\lambda_{\perp}$ . The relationship between parallel and perpendicular diffusion coefficients over solar cycles depends on the details of variations of  $\delta B$  and  $B$ . It is noted that [Chhiber et al. \(2017\)](#) also studied the influence of solar activity on CR parallel and perpendicular diffusion with the modeling background magnetic field and turbulence, they found that an increasing  $\delta B$  leads to a decrease in  $\lambda_{\parallel}$  and an increase in  $\lambda_{\perp}$ . We think it is reasonable to have different relationship between parallel and perpendicular diffusion coefficients using different  $\delta B$  and  $B$ .

The real solar modulation boundary might be located beyond the heliopause (e.g., [Zhang et al. 2015](#)). Voyager 1 was assumed to have reached the very local interstellar medium in August 2012

(Webber & McDonald 2013), the very local interstellar spectrum (LIS) is able to be constructed using proton flux of Voyager 1 and that of PAMELA with energy larger than 30 GeV where the modulation effects can be neglected (Potgieter 2013; Vos & Potgieter 2015; Bisschoff & Potgieter 2016). In addition, observations (Stone et al. 2005, 2008) indicated that Voyager 1 and 2 reached the TS in 2004 and 2007 at about 94.0 AU and 83.7 AU, respectively. Thus the TS may have an asymmetric structure and a temporal position. The asymmetric structure can also be seen in some MHD models (e.g., Opher et al. 2009; Florinski & Pogorelov 2009), and has identifiable modulation effects on GCRs (Langner & Potgieter 2005). The variations of the solar wind speed and density can result in a time-dependent TS position (see, e.g., Whang et al. 1995, 2004; Wang & Belcher 1999; Webber 2005; Webber & Intriligator 2011; Washimi et al. 2011; Richardson & Wang 2011, 2012), and the TS position shows a latitude dependence (Webber & Intriligator 2011; Washimi et al. 2011). However, the temporal profiles of the TS position shown by these theoretical works are somehow different. Thus the realistic TS position is complicated to be constructed considering its time and latitude dependence. As has been shown by the results of Manuel et al. (2014), the TS and heliopause positions are important parameters in the modulation of GCRs. Considering a fixed heliopause position and a symmetric heliosphere, Manuel et al. (2015) studied the modulation effects of a time-varying sinusoidal TS position and a fixed one. Little difference was shown for the modulation of GCRs near Earth, but the time-dependent TS position (i.e., the time-dependent inner heliosheath thickness) had significant effects on the temporal variation of GCR intensity near TS. Since modulation effects in the outer heliosphere have not been included in our modulation model, following Qin & Shen (2017) we set a symmetric outer boundary of modulation inside the termination shock at 85 au and use an input spectrum according to the observations of Voyager 2 at 85 au from Webber et al. (2008). Following Zhang (1999), we express the GCR source at 85 au as follows,

$$j_s = j_0 p_0^{2.6} p (m_0^2 c^2 + p^2)^{-1.8} \quad (18)$$

where  $j_0 = 1.17 \times 10^4 \text{ m}^{-2} \text{ s}^{-1} \text{ sr}^{-1} (\text{GeV}/\text{nuc})^{-1}$  to fit Voyager 2 observations (Qin & Shen 2017),  $p_0 = 1 \text{ GeV}/c$  and  $m_0$  means the rest mass of a proton.

In this work, we use the time-backward Markov stochastic process method which is proposed by [Zhang \(1999\)](#) to solve the well known Parker transport equation. The Parker transport equation can be written in terms of a set of equivalent stochastic differential equations (SDEs) given by ([Zhang 1999](#); [Pei et al. 2010b](#); [Strauss et al. 2011](#); [Kopp et al. 2012](#))

$$dx_i = A_i(x_i)ds + \sum_j B_{ij}(x_i) \cdot dW_j, \quad (19)$$

with  $i \in (r, \theta, \phi, p)$ ,  $x_i$  are the Ito processes ([Zhang 1999](#)),  $s$  is the backward time, and  $dW_i$  satisfy a Wiener process given by the standard normal distribution ([Pei et al. 2010b](#); [Strauss et al. 2011](#)). For a general HMF with a meridional component, the matrix components  $B_{ij}$  are given by [Pei et al. \(2010b\)](#) (see also [Kopp et al. 2012](#)). For the components of vector  $\mathbf{A}$  and the specific SDEs in spherical coordinate, please refer to [Qin & Shen \(2017\)](#). We trace a number of pseudo-particles from the observation location outward to the outer boundary and get particle intensities with the GCR source spectrum. We assume a locally static heliosphere for each month, and interplanetary conditions (e.g.,  $V_{sw}$ ,  $B$ ,  $\delta B$ ,  $\alpha$ ,  $P_A$ ) in position  $\mathbf{r}$  at time  $t$  are decided by the states at the source surface  $r_s$  at an earlier time ([Potgieter et al. 2014](#)), thus we use a time-delayed heliosphere according to [Qin & Shen \(2017\)](#). We solve the TPE at monthly intervals.

#### 4. MODELING RESULTS

While studying the modulation of GCR over solar cycles, we still need to know the characteristics of energy spectra both in solar minimum and solar maximum. In our previous work ([Qin & Shen 2017](#)), we have successfully reproduced the proton spectra observed by PAMELA measurements as a function of time in the past  $A < 0$  solar minimum. However, modeling work during solar maximum remains a challenge. During the maximum phase of each cycle, the heliosphere is more complex due to the high-level solar activities, and the Sun's polar magnetic field changes sign (i.e., the sign of  $A$ ) frequently. For simplification, we assume the solar wind speed has no latitudinal component during solar maximum according to the observations of Ulysses ([Heber & Potgieter 2006](#)) and use a time delayed heliosphere ([Qin & Shen 2017](#)). In addition, for each pseudo-particle in each time step, the solar magnetic field polarity  $A$  is decided as  $A = 1$  or  $A = -1$  randomly according to the percentage  $P_A$ .

Figure 6 shows an example of the modulated proton energy spectra near solar maximum in 1990 (red line) and near solar minimum in 1997 (blue line). Black line represents the GCR source used in this work (Qin & Shen 2017). Blue and sky blue solid circles mean IMP 8 observations in 1997 from Webber & Higbie (2003) and BESS magnetic spectrometer observations in 1997 from Shikaze et al. (2007), respectively. Red solid circles refer to yearly averaged GCR proton flux observed by IMP 8 in 1990. Note that the original 30-minute resolution proton flux data (from CDAWeb: [cdaweb.sci.gsfc.nasa.gov](http://cdaweb.sci.gsfc.nasa.gov)) has been processed to get the GCR background using the despiking algorithm (Qin et al. 2012). The computed energy spectrum in solar maximum is harder than that in solar minimum, and the results of our model are consistent with these GCR observations. In this figure, the spectra observed by Voyager 1 (magenta circles) and Voyager 2 (gray circles) in 1998 reported by Webber et al. (2006) are shown even softer than the GCR source, which can be hardly reproduced by our model. Therefore, in the following, instead to study the energy spectra, we only focus on the time-dependent modulation of GCRs. Furthermore, for GCRs observed by Voyager 1 & 2 along their trajectories, we only study the lower energy ( $\sim 140$  MeV) channel of GCRs.

Figure 7 shows the monthly averaged 230 – 327 MeV proton intensity observed by IMP 8 as a function of time from 1978 to 2001 (gray line) and the computed monthly 274 MeV proton intensity (red line) at Earth for period 1978-2016. Gray triangles represent yearly 292 MeV proton flux observed by SOHO/EPHIN (Kühl et al. 2016). GCR observations are always contaminated by solar cosmic rays (e.g., Shen & Qin 2016) which are mainly manifested as large spikes in the temporal profile of GCRs. The phase-space thresholding method (see, e.g., Qin et al. 2012) is used to deal with the IMP 8 data for a pure GCR background. The profiles of IMP 8 and SOHO/EPHIN data show a clear 11-year cycle which is anti-correlated with the variations of solar activity. Typical peaked and plateau-like time profiles can be seen for  $A > 0$  and  $A < 0$  solar cycles, respectively. During solar maxima, step-like decreases were observed. The modulation magnitude in solar maximum 2012-2014 is much smaller than previous two solar maxima due to lower solar activity level which can be illustrated by the sunspot number from WDC-SILSO ([sidc.be/silso/](http://sidc.be/silso/)). Zhao & Zhang (2015) studied the GCR heavy-ion flux in the weak solar maximum 2014. Comparing with observations in the last solar maximum 2002, they found the elemental intensities of all heavy nuclei in 2014 to be  $\sim 40\%$  higher, which were attributed to the weak modulation associated with low solar activity levels

in 2014. The computed monthly averaged 274 MeV proton intensity at Earth is consistent with spacecraft observations. The 11-year cycle and the step-like magnitude during solar maximum has been reproduced. The model also gives peaked and plateau-like temporal profiles during the  $A > 0$  and  $A < 0$  solar minimum, respectively. Small peaks on the temporal profile of modeling result are caused by the violent changes of input parameters, especially the variation of magnetic turbulence magnitude. In the period of 1981-1982, the computed result is higher than the observation, which may be caused by the increased perpendicular diffusion coefficient as has been shown in the second panel of Figure 5. The magnetic turbulence magnitude is relatively low in the first half of 1984, which causes a peak in the temporal profile of parallel mean-free path. Thus the computed result in 1984 is relatively higher than the observation, and the following sharp decrease of the computed result is attributable to large spikes exist in IMF and magnetic turbulence. Such phenomenon can also be seen in 1991 and 2003. The computed result has a sharp increase in 2013, while the observed proton intensity keep decreasing until 2014. Despite the relatively larger perpendicular mean-free path in 2013, the solar polar field also depicts some unusual variation characteristics. From the bottom panel of Figure 2 we can see that  $P_A = 1$  from June 2013 to December 2013, and this can be an important factor leading to the sharp increase in GCR intensity. Note that it is hard to use our model to reproduce the temporal profile of the observed galactic proton intensity precisely, because the modeling heliosphere is oversimplified (e.g., the Parker HMF and the turbulence model). Nonetheless, the reproduced 11-year cycle and variation amplitudes over solar maximum can help us understand the physical processes of solar modulation. To have a better scenario, we show the yearly averaged modeling result in the following work.

Ulysses was launched on October 6, 1990 and orbited around the Sun with the latitude varying from  $-80^\circ$  to  $80^\circ$  and the solar distance ranging from  $\sim 1$  au to  $\sim 5$  au (Heber et al. 2009). The Kiel Electron Telescope (KET) on board Ulysses measured electrons in the energy range from  $\sim 3$  MeV to above 300 MeV, and protons and helium nuclei in the energy range from  $\sim 5$  MeV/nuc to above 2 GeV/nuc (Simpson et al. 1992). The data of KET coincidence channel K12, which measures protons with energy in 0.25 – 2.0 GeV, has been used to study the modulation of GCR outside the solar ecliptic plane in many works (see, e.g., Ndiitwani et al. 2005; Vos & Potgieter 2016; Boschini et al. 2017b). However, different works used different mono-energetic bin to represent this channel, e.g., 1.08 GeV (Rastoin et al. 1996), 2.5 GV (i.e., 1.73

GeV, Ndiitwani et al. 2005; Heber et al. 2009; Manuel et al. 2014) and 2.2 GeV (Boschini et al. 2017b). As the KET observations are integrated over a large energy interval (de Simone et al. 2011), perhaps it is better to weight the model results of several energy bins with the Ulysses response function and then combine them together (Boschini et al. 2017b). Heber et al. (2009) got the 1 au equivalent count rates for this channel by correcting the proton intensity with the global spatial gradients of GCR protons, and one can get the 1 au equivalent GCR proton flux with the corresponding response factor. In addition, the precise cosmic-ray spectra measured by the PAMELA instrument can help us roughly estimate the effective energy of KET coincidence channel K12. In Figure 8, the black solid line means monthly averaged 0.25 – 2.0 GeV proton flux observed by Ulysses. Note that the original daily count rates from the Ulysses Final Archive ([ufa.esac.esa.int/ufa](http://ufa.esac.esa.int/ufa)) are divided by the corresponding response factor to get the proton flux. The dashed-dotted line represents the 1 au equivalent 0.25 – 2.0 GeV proton flux, and the relevant count rates are digitized from Figure 5 in Heber et al. (2009). The 1.2 GeV proton flux observed by SOHO/EPHIN (Kühl et al. 2016) and PAMELA (Adriani et al. 2013) are shown as magenta triangles and green circles, respectively. The 1 au equivalent GCR proton flux roughly matches the 1.2 GeV GCR proton observations, and one can use 1.2 GeV to represent Ulysses/KET channel K12. Therefore, we will compute the 1.2 GeV proton flux along the trajectory of Ulysses to compare with the Ulysses K12 measurements.

Top panel of Figure 9 illustrates the trajectory of Ulysses. Black line is the temporal profile of radial distance varying from 1.4 au to 5.4 au. Red line means the heliographic latitude of Ulysses as a function of time. There are three fast latitude scans when the latitude varying quickly from  $-80^\circ$  to  $80^\circ$  (Heber et al. 2009). Black line in the bottom panel shows the intensity of 0.25 – 2.0 GeV protons observed by Ulysses/KET, the variations of which are caused by solar cycles as well as the spatial changes of Ulysses. Red circles in the bottom panel are computed yearly averaged 1.2 GeV proton intensities along the trajectory of Ulysses. Generally speaking, the numerical modeling results are consistent with the observations. The modulation model reproduces a plateau-like temporal profile during the  $A > 0$  cycle, and the results during solar maximum are also consistent with observations. However, as we consider a mono-energetic bin, the modeling results can not couple with observations all the time. In period 2004-2005, modeling results are lower than observations to some extent. As has been shown in the bottom panel of Figure 1, turbulence in period

2004-2005 is much higher than previous two years, which causes smaller diffusion coefficients, and further result in a lower computed proton intensity. The modeling results show a sharp increase after 2005 due to the obviously decreases in magnetic turbulence, magnetic field and tilt angle after 2005.

Figure 10 is another example of numerical results along the trajectory of Voyager 1. As the modulation boundary is set at 85 au, we only study the time-dependent modulation from 1978 to 2000. Top panel shows the trajectory of Voyager 1, black line means the radial distance, red line is the temporal profile of heliographic latitude varying from  $-5.5^\circ$  to  $33.7^\circ$ . Bottom panel illustrates the observed 133 – 155 MeV and the computed yearly averaged 143 MeV proton intensities as a function of time. Note that observation data shown in this figure are monthly averaged using daily data from GSFC/SPDF OMNIWeb interface ([omniweb.gsfc.nasa.gov/](http://omniweb.gsfc.nasa.gov/)). A peaked temporal profile was not observed during the  $A < 0$  solar minimum, neither did the observed proton intensity show obvious decreases in 1988 as expected, because Voyager 1 experienced both corotating merged interaction regions and rarefaction regions during 1988. The corotating merged interaction regions and rarefaction regions had equal and opposite effects on the variation of cosmic-ray intensities (Burlaga et al. 1993). The balance lasted until Voyager 1 encountered a GMIR in 1989, meanwhile, the instrument observed a large decrease in proton intensity. These complicated structures can not be reproduced by the modified Parker HMF. Step-like decreases and increases were observed during solar maxima, and the observed decrease/increase amplitudes tend to be smaller while the spacecraft moving toward the modulation boundary. Such phenomenon is also reproduced by the model to some extent. Modeling results near Earth are larger than observations in periods 1981-1982 and 1991-1992, and such effects are magnified in the distant heliosphere. Along the trajectories of Voyager 1 & 2, the predicted magnetic turbulence magnitude is a little lower than observations in period 1981-1986 (see Figure 4 in Qin & Shen 2017), which might be a reason for the larger modeling result during this period.

Figure 11 is similar to Figure 10 except that it is for Voyager 2. The heliographic latitude of Voyager 2 varies from  $\sim -5^\circ$  to  $\sim 23^\circ$  and the radial distance ranges from  $\sim 2$  au to  $\sim 65$  au during this period. Note that observation data shown in the bottom panel of Figure 11 are monthly averaged using daily data from GSFC/SPDF OMNIWeb interface ([omniweb.gsfc.nasa.gov/](http://omniweb.gsfc.nasa.gov/)). During the period of 1986-1988 ( $A < 0$ ), proton mainly transport along the wavy HCS. Voyager 2 moved out near the ecliptic plane while Voyager

1 was above the sector zone of HCS (Burlaga et al. 2002), thus proton intensity measured by Voyager 2 was larger than that of Voyager 1 (Manuel et al. 2011a). The observed proton flux peaked in the period of 1998 – 1999 and had a significant decrease which was produced by a GMIR in the second quarter of the year 2000 (Burlaga et al. 2003). The second step-decrease was observed at the end of the year 2000, produced by the arrival of a large GMIR from the Bastille day event at the Earth in 2000 (Webber et al. 2002). Such step-decreases were also observed by Voyager 1. Despite the periods discussed above, the computed results are consistent with the spacecraft observations. In the period of 1998-1999, the results of our model are lower than observations, and provide a sharp decrease after 1998, which is about one year later comparing with the modeling results near Earth (see Figure 7). The temporal profiles of proton flux observed by Voyager 1 and Voyager 2 are nearly the same in the period of 1998-2000. However, the profiles of the computed results along the trajectories of Voyager 1 and Voyager 2 are totally different with the modeling results of Voyager 1 being closer to the observations. If a more realistic heliosphere is incorporated in our model, the modeling results might fit the observations better.

## 5. DISCUSSION AND CONCLUSIONS

In this work, we establish a numerical model to study the modulation of GCRs over several solar cycles. As the Parker HMF gives a low magnitude in the polar regions at large radial distance, we modify the expression according to Jokipii & Kota (1989). New diffusion coefficients model given by Qin & Zhang (2014) is applied. Magnetic turbulence quantities throughout the heliosphere are important parameters in this diffusion coefficients model. We only consider the variability of magnetic turbulence magnitude  $\delta B$  for simplicity, which is assumed as a function of spatial location and the tilt angle of HCS (Qin & Shen 2017). Then we establish a time-dependent diffusion coefficients model with some observations at 1 au as the input parameters. The effects of HMF modification on particle drifts and diffusion are also considered. We assume the Sun's magnetic polarity as random during solar maximum with the possibility of  $A > 0$  decided by the percentage of the north solar polar magnetic field being outward and south solar pole magnetic field being inward. In addition, a realistic time delayed heliosphere described in Qin & Shen (2017) is incorporated in our numerical model.

Firstly we study the modulated GCR proton spectra near solar minimum and maximum. The computed spectrum near solar maximum turned out to be harder than that of solar minimum, which are consistent with observations of IMP8 and BESS, etc. However, the proton spectra observed by Voyager 1 and Voyager 2 are hard to be reproduced by our model, because they are even softer than the GCR source in our model. Thus we focus on the time-dependent modulation of GCRs with single individual energy channels instead of the spectra. In addition, we only study the low energy channel of GCRs along the trajectories of Voyager 1 & 2.

We compute monthly 274 MeV proton intensities at Earth from 1978 to 2016. Comparing with the 230-327 MeV proton intensity observations of IMP 8 and the observations of SOHO/EPHIN, we believe that our model has reproduced the  $\sim 11$ - and  $\sim 22$ -year cycles of solar modulation. The step-like magnitude of GCR intensity during solar maximum is also consistent with the observations. The 1 au equivalent proton intensity with energy ranges in 0.25-2.0 GeV (Ulysses K12) from Heber et al. (2009) roughly matches the 1.2 GeV proton observations from PAMELA and SOHO/EPHIN measurements. Therefore, 1.2 GeV can be used to represent the Ulysses K12 channel. We utilize the numerical model to calculate 1.2 GeV proton intensity along the trajectory of Ulysses. Modeling results are in close agreement with the observations. Due to the larger magnetic turbulence magnitude and smaller radial decay index  $S$ , the diffusion coefficients are much smaller in the heliosphere during the solar maximum and it is harder for energetic particles to participate in the inner heliosphere. Thus the numerical model gives large decrease during solar maximum. That is also the reason why the computed proton intensity is smaller than observations in the period of 2004-2005. We also study long-term modulation of GCRs in low energy channel along the trajectories of Voyager 1 & 2. The numerical results are also consistent with the observations, but the model gets larger results in the period of 1981-1986 and 1991-1992, during which perhaps larger turbulence level is needed in the distant heliosphere. Besides, from Figure 2 in Zhao et al. (2017), the 2D and slab turbulence energy decrease with the radial distance from 1 to 75 au. However, because of the pick-up ion driving turbulence, the decay slows down after about 10 au.

For the characteristics of magnetic turbulence, we only consider the time and spatial dependence of IMF strength and magnetic turbulence magnitude. The values of  $\lambda_{slab}/\lambda_{2D}$  and  $E_{slab}/E_{total}$  are set as con-

stants. Theoretical works (see, e.g., [Oughton et al. 2011](#); [Engelbrecht & Burger 2013](#); [Zank et al. 2017](#)) have shown more complicated variation characteristics, and the values of  $\lambda_{slab}/\lambda_{2D}$  and  $E_{slab}/E_{total}$  may change with solar activity. In addition, TRST is a phenomenological model without considering the physical processes of turbulence transport in the heliosphere, and the results of TRST can not couple with the real condition all the time. Incorporating the results of TTMs (e.g., [Zank et al. 2017](#)) may help us to study the modulation of GCRs. However, it still needs a further study to depict turbulence quantities over solar cycles. Modulation effects of heliosheath are not considered in this work. Inferring from the work of [Manuel et al. \(2015\)](#), the time-dependent inner heliosheath thickness has significant modulation effects on GCR intensities near TS. Thus, incorporating the modulation effects of heliosheath and a time-dependent TS position can improve the modeling results along the trajectories of Voyager 1 & 2. Following [Qin \(2007\)](#), the time delayed modified Parker HMF and the solar wind speed are used to establish a realistic heliosphere. However, the structure of the real heliosphere is much more complicated. Thus the computed results are not consistent with observations precisely.

Consequently, the time-dependent diffusion coefficients model based on the work of [Qin & Zhang \(2014\)](#) allow us to study long-term cosmic-ray modulation in the inner heliosphere, and all input parameters can be obtained from observations at Earth. In the future, we will consider the modulation of GCRs outside the termination shock, so we can change the modulation boundary much larger than 85 au and get numerical results along trajectories of Voyager 1 & 2 after 2001. In addition, we will study the effects of modulation when particles transport across a sectored magnetic field in the out heliosphere ([Florinski 2011](#); [Florinski et al. 2012](#)). Furthermore, we would study the modulation of GCR heavy-ions over solar cycles with spacecraft observations and numerical calculations. At last, we would work on the study of proton spectra observed by Voyager 1 and Voyager 2 in the heliosphere.

We are partly supported by grants NNSFC 41374177 and NNSFC 41574172. We used data from the Wilcox Solar Observatory ([wso.stanford.edu](http://wso.stanford.edu)), GSFC/SPDF OMNIWeb interface ([omniweb.gsfc.nasa.gov](http://omniweb.gsfc.nasa.gov)), NASA CDAWeb ([cdaweb.sci.gsfc.nasa.gov](http://cdaweb.sci.gsfc.nasa.gov)) and Ulysses Final Archive ([ufa.esac.esa.int/ufa](http://ufa.esac.esa.int/ufa)).

The work was carried out at National Supercomputer Center in Tianjin, and the calculations were performed on TianHe-1 (A).

## REFERENCES

- Adhikari, L., Zank, G. P., Hu, Q., & Dosch, A. 2014, *ApJ*, 793, 52
- Adhikari, L., Zank, G. P., Hunana, P., et al. 2017, *ApJ*, 841, 85
- Adriani, O., Barbarino, G. C., Bazilevskaya, G. A., et al. 2013, *ApJ*, 765, 91
- Alania, M. V., Baranov, D. G., Tyasto, M. I., & Vernova, E. S. 2001, *Advances in Space Research*, 27, 619
- Alania, M. V., Modzelewska, R., & Wawrzynczak, A. 2011, *SoPh*, 270, 629
- Bieber, J. W., & Matthaeus, W. H. 1997, *ApJ*, 485, 655
- Bieber, J. W., Matthaeus, W. H., Smith, C. W., et al. 1994, *ApJ*, 420, 294
- Bischoff, D., & Potgieter, M. S. 2016, *Ap&SS*, 361, 48
- Bobik, P., Boella, G., Boschini, M. J., et al. 2012, *ApJ*, 745, 132
- Bobik, P., Boella, G., Boschini, M. J., et al. 2013, *Advances in Astronomy*, 2013, 793072
- Boschini, M. J., Della Torre, S., Gervasi, M., La Vacca, G., & Rancoita, P. G. 2017a, *ArXiv e-prints*, arXiv:1704.03733
- Boschini, M. J., Della Torre, S., Gervasi, M., et al. 2017b, *ApJ*, 840, 115
- Breech, B., Matthaeus, W. H., Minnie, J., et al. 2008, *Journal of Geophysical Research (Space Physics)*, 113, A08105
- Burger, R. A., Krüger, T. P. J., Hitge, M., & Engelbrecht, N. E. 2008, *ApJ*, 674, 511
- Burger, R. A., & Potgieter, M. S. 1989, *ApJ*, 339, 501
- Burger, R. A., Potgieter, M. S., & Heber, B. 2000, *J. Geophys. Res.*, 105, 27447
- Burger, R. A., & Visser, D. J. 2010, *ApJ*, 725, 1366
- Burlaga, L. F., McDonald, F. B., & Ness, N. F. 1993, *J. Geophys. Res.*, 98, 1
- Burlaga, L. F., Ness, N. F., McDonald, F. B., Richardson, J. D., & Wang, C. 2003, *ApJ*, 582, 540
- Burlaga, L. F., Ness, N. F., Wang, Y.-M., & Sheeley, N. R. 2002, *Journal of Geophysical Research (Space Physics)*, 107, 1410
- Candia, J., & Roulet, E. 2004, *JCAP*, 10, 007
- Cane, H. V. 2000, *SSRv*, 93, 55
- Chhiber, R., Subedi, P., Usmanov, A. V., et al. 2017, *ApJS*, 230, 21
- Cliver, E. W., Richardson, I. G., & Ling, A. G. 2013, *SSRv*, 176, 3
- Dasso, S., Milano, L. J., Matthaeus, W. H., & Smith, C. W. 2005, *ApJL*, 635, L181
- de Simone, N., di Felice, V., Gieseler, J., et al. 2011, *Astrophysics and Space Sciences Transactions*, 7, 425
- Dosch, A., Adhikari, L., & Zank, G. P. 2013, *Solar Wind 13*, 1539, 155
- Effenberger, F., Fichtner, H., Scherer, K., et al. 2012, *ApJ*, 750, 108
- Engelbrecht, N. E., & Burger, R. A. 2013, *ApJ*, 772, 46
- Engelbrecht, N. E., Strauss, R. D., le Roux, J. A., & Burger, R. A. 2017, *ApJ*, 841, 107
- Ferreira, S. E. S., & Potgieter, M. S. 2004, *ApJ*, 603, 744
- Fisk, L. A. 1996, *J. Geophys. Res.*, 101, 15547

- Fisk, L. A., & Schwadron, N. A. 1995, *J. Geophys. Res.*, 100, 7865
- Florinski, V. 2011, *Advances in Space Research*, 48, 308
- Florinski, V., Alouani-Bibi, F., Kota, J., & Guo, X. 2012, *ApJ*, 754, 31
- Florinski, V., & Pogorelov, N. V. 2009, *ApJ*, 701, 642
- Forsyth, R. J., Balogh, A., Smith, E. J., Erdős, G., & McComas, D. J. 1996, *J. Geophys. Res.*, 101, 395
- Giacalone, J., & Jokipii, J. R. 1999, *ApJ*, 520, 204
- Gil, A., & Mursula, K. 2017, *A&A*, 599, A112
- Gleeson, L. J., & Axford, W. I. 1968, *ApJ*, 154, 1011
- Gleeson, L. J., & Urch, I. H. 1971, *Ap&SS*, 11, 288
- Guo, X., & Florinski, V. 2016, *ApJ*, 826, 65
- Hattingh, M. 1998, PhD thesis, Potchefstroom Univ., (1998)
- Heber, B., Kopp, A., Gieseler, J., et al. 2009, *ApJ*, 699, 1956
- Heber, B., & Potgieter, M. S. 2006, *SSRv*, 127, 117
- Hunana, P., & Zank, G. P. 2010, *ApJ*, 718, 148
- Jokipii, J. R. 1966, *ApJ*, 146, 480
- Jokipii, J. R. 1993, *International Cosmic Ray Conference*, 3, 497
- Jokipii, J. R., & Kota, J. 1989, *Geophys. Res. Lett.*, 16, 1
- Jokipii, J. R., Levy, E. H., & Hubbard, W. B. 1977, *ApJ*, 213, 861
- Kopp, A., Büsching, I., Strauss, R. D., & Potgieter, M. S. 2012, *Computer Physics Communications*, 183, 530
- Kota, J., & Jokipii, J. R. 1983, *ApJ*, 265, 573
- Kota, J., & Jokipii, J. R. 2001, *International Cosmic Ray Conference*, 9, 3577
- Kühl, P., Gómez-Herrero, R., & Heber, B. 2016, *SoPh*, 291, 965
- Langner, U. W. 2004, PhD thesis, Potchestroom University
- Langner, U. W., & Potgieter, M. S. 2005, *ApJ*, 630, 1114
- Le Roux, J. A., & Potgieter, M. S. 1990, *ApJ*, 361, 275
- Le Roux, J. A., & Potgieter, M. S. 1995, *ApJ*, 442, 847
- Lockwood, J. A. 1971, *SSRv*, 12, 658
- Manuel, R., Ferreira, S. E. S., & Potgieter, M. S. 2011a, *Advances in Space Research*, 48, 874
- Manuel, R., Ferreira, S. E. S., & Potgieter, M. S. 2014, *SoPh*, 289, 2207
- Manuel, R., Ferreira, S. E. S., & Potgieter, M. S. 2015, *ApJ*, 799, 223
- Manuel, R., Ferreira, S. E. S., Potgieter, M. S., Strauss, R. D., & Engelbrecht, N. E. 2011b, *Advances in Space Research*, 47, 1529
- Marsch, E., & Tu, C.-Y. 1989, *Journal of Plasma Physics*, 41, 479
- Matthaeus, W. H., Bieber, J. W., Ruffolo, D., Chuychai, P., & Minnie, J. 2007, *ApJ*, 667, 956
- Matthaeus, W. H., Goldstein, M. L., & Roberts, D. A. 1990a, *J. Geophys. Res.*, 95, 20673
- Matthaeus, W. H., Goldstein, M. L., & Roberts, D. A. 1990b, *J. Geophys. Res.*, 95, 20673
- Matthaeus, W. H., Qin, G., Bieber, J. W., & Zank, G. P. 2003, *ApJL*, 590, L53
- Matthaeus, W. H., Zank, G. P., Smith, C. W., & Oughton, S. 1999, *Physical Review Letters*, 82, 3444

- McComas, D. J., Elliott, H. A., Gosling, J. T., et al. 2002, *Geophys. Res. Lett.*, 29, 4
- McDonald, F. B. 1998, *SSRv*, 83, 33
- Minnie, J., Bieber, J. W., Matthaeus, W. H., & Burger, R. A. 2007, *ApJ*, 670, 1149
- Ndiitwani, D. C., Ferreira, S. E. S., Potgieter, M. S., & Heber, B. 2005, *Annales Geophysicae*, 23, 1061
- Ngobeni, M. D., & Potgieter, M. S. 2014, *Advances in Space Research*, 53, 1634
- Nndanganeni, R. R., & Potgieter, M. S. 2016, *Advances in Space Research*, 58, 453
- Opher, M., Richardson, J. D., Toth, G., & Gombosi, T. I. 2009, *SSRv*, 143, 43
- Osman, K. T., & Horbury, T. S. 2007, *ApJL*, 654, L103
- Oughton, S., Matthaeus, W. H., Smith, C. W., Breech, B., & Isenberg, P. A. 2011, *Journal of Geophysical Research (Space Physics)*, 116, A08105
- Parker, E. N. 1958, *ApJ*, 128, 664
- Parker, E. N. 1965, *Planet. Space Sci.*, 13, 9
- Pei, C., Bieber, J. W., Breech, B., et al. 2010a, *Journal of Geophysical Research (Space Physics)*, 115, A03103
- Pei, C., Bieber, J. W., Burger, R. A., & Clem, J. 2010b, *Journal of Geophysical Research (Space Physics)*, 115, A12107
- Perko, J. S., & Fisk, L. A. 1983, *J. Geophys. Res.*, 88, 9033
- Perri, S., & Balogh, A. 2010, *Geophys. Res. Lett.*, 37, L17102
- Potgieter, M. 2013, *Living Reviews in Solar Physics*, 10, arXiv:1306.4421
- Potgieter, M. S. 2000, *J. Geophys. Res.*, 105, 18295
- Potgieter, M. S. 2017, *Advances in Space Research*, 60, 848
- Potgieter, M. S., & Le Roux, J. A. 1992, *ApJ*, 386, 336
- Potgieter, M. S., Le Roux, J. A., & Burger, R. A. 1989, *J. Geophys. Res.*, 94, 2323
- Potgieter, M. S., Le Roux, J. A., Burlaga, L. F., & McDonald, F. B. 1993, *ApJ*, 403, 760
- Potgieter, M. S., Mwiinga, N., Ferreira, S. E. S., Manuel, R., & Ndiitwani, D. C. 2013, *Journal of Advanced Research*, 4, 259
- Potgieter, M. S., Vos, E. E., Boezio, M., et al. 2014, *SoPh*, 289, 391
- Potgieter, M. S., Vos, E. E., Munini, R., Boezio, M., & Di Felice, V. 2015, *ApJ*, 810, 141
- Qin, G. 2007, *ApJ*, 656, 217
- Qin, G., Matthaeus, W. H., & Bieber, J. W. 2002, *ApJL*, 578, L117
- Qin, G., & Shen, Z.-N. 2017, *ApJ*, 846, 56
- Qin, G., & Zhang, L.-H. 2014, *ApJ*, 787, 12
- Qin, G., Zhao, L.-L., & Chen, H.-C. 2012, *ApJ*, 752, 138
- Raath, J. L., Potgieter, M. S., Strauss, R. D., & Kopp, A. 2016, *Advances in Space Research*, 57, 1965
- Rastoin, C., Ferrando, P., Raviart, A., et al. 1996, *A&A*, 307, 981
- Richardson, I. G. 2004, *SSRv*, 111, 267
- Richardson, I. G., Cane, H. V., & Wibberenz, G. 1999, *J. Geophys. Res.*, 104, 12549
- Richardson, I. G., Wibberenz, G., & Cane, H. V. 1996, *J. Geophys. Res.*, 101, 13483
- Richardson, J. D., & Wang, C. 2011, *ApJL*, 734, L21
- Richardson, J. D., & Wang, C. 2012, *ApJL*, 759, L19

- Roberts, D. A., Giacalone, J., Jokipii, J. R., Goldstein, M. L., & Zepp, T. D. 2007, *Journal of Geophysical Research (Space Physics)*, 112, A08103
- Shalchi, A., Bieber, J. W., & Matthaeus, W. H. 2004, *ApJ*, 604, 675
- Sheeley, N. R., Wang, Y.-M., Hawley, S. H., et al. 1997, *ApJ*, 484, 472
- Shen, Z.-N., & Qin, G. 2016, *Journal of Geophysical Research: Space Physics*, 121, 10712
- Shikaze, Y., Haino, S., Abe, K., et al. 2007, *Astroparticle Physics*, 28, 154
- Shiota, D., Zank, G. P., Adhikari, L., et al. 2017, *ApJ*, 837, 75
- Simpson, J. A., Zhang, M., & Bame, S. 1996, *ApJL*, 465, L69
- Simpson, J. A., Anglin, J. D., Balogh, A., et al. 1992, *A&AS*, 92, 365
- Smith, C. W., & Bieber, J. W. 1991, *ApJ*, 370, 435
- Smith, C. W., Matthaeus, W. H., Zank, G. P., et al. 2001, *J. Geophys. Res.*, 106, 8253
- Stawicki, O. 2005, *ApJ*, 624, 178
- Sternal, O., Engelbrecht, N. E., Burger, R. A., et al. 2011, *ApJ*, 741, 23
- Stone, E. C., Cummings, A. C., McDonald, F. B., et al. 2005, *Science*, 309, 2017
- Stone, E. C., Cummings, A. C., McDonald, F. B., et al. 2008, *Nature*, 454, 71
- Strauss, R. D., Potgieter, M. S., Büsching, I., & Kopp, A. 2011, *ApJ*, 735, 83
- Strauss, R. D., Potgieter, M. S., Büsching, I., & Kopp, A. 2012, *Ap&SS*, 339, 223
- Strauss, R. D. T., Dresing, N., & Engelbrecht, N. E. 2017, *The Astrophysical Journal*, 837, 43
- Tautz, R. C., & Shalchi, A. 2012, *ApJ*, 744, 125
- Teufel, A., & Schlickeiser, R. 2002, *A&A*, 393, 703
- Teufel, A., & Schlickeiser, R. 2003, *A&A*, 397, 15
- Usmanov, A. V., Goldstein, M. L., & Matthaeus, W. H. 2014, *ApJ*, 788, 43
- Usmanov, A. V., Goldstein, M. L., & Matthaeus, W. H. 2016, *ApJ*, 820, 17
- Usmanov, A. V., Matthaeus, W. H., Breech, B. A., & Goldstein, M. L. 2011, *ApJ*, 727, 84
- Vos, E. E., & Potgieter, M. S. 2015, *ApJ*, 815, 119
- Vos, E. E., & Potgieter, M. S. 2016, *SoPh*, 291, 2181
- Wang, C., & Belcher, J. W. 1999, *J. Geophys. Res.*, 104, 549
- Washimi, H., Zank, G. P., Hu, Q., et al. 2011, *MNRAS*, 416, 1475
- Wawrzynczak, A., & Alania, M. V. 2010, *Advances in Space Research*, 45, 622
- Webber, W. R. 2005, *Journal of Geophysical Research (Space Physics)*, 110, A10103
- Webber, W. R., Cummings, A. C., McDonald, F. B., et al. 2008, *Journal of Geophysical Research (Space Physics)*, 113, A10108
- Webber, W. R., & Higbie, P. R. 2003, *Journal of Geophysical Research (Space Physics)*, 108, 1355
- Webber, W. R., & Intriligator, D. S. 2011, *Journal of Geophysical Research (Space Physics)*, 116, A06105
- Webber, W. R., & Lockwood, J. A. 1993, *J. Geophys. Res.*, 98, 21

- Webber, W. R., & McDonald, F. B. 2013, *Geophys. Res. Lett.*, 40, 1665
- Webber, W. R., McDonald, F. B., Cummings, A. C., et al. 2006, *Journal of Geophysical Research (Space Physics)*, 111, A08107
- Webber, W. R., McDonald, F. B., Lockwood, J. A., & Heikkila, B. 2002, *Geophys. Res. Lett.*, 29, 15
- Weygand, J. M., Matthaeus, W. H., Dasso, S., & Kivelson, M. G. 2011, *Journal of Geophysical Research (Space Physics)*, 116, A08102
- Weygand, J. M., Matthaeus, W. H., Dasso, S., et al. 2009, *Journal of Geophysical Research (Space Physics)*, 114, A07213
- Whang, Y. C., Burlaga, L. F., & Ness, N. F. 1995, *J. Geophys. Res.*, 100, 17015
- Whang, Y. C., Burlaga, L. F., Wang, Y.-M., & Sheeley, N. R. 2004, *Geophys. Res. Lett.*, 31, L03805
- Wiengarten, T., Fichtner, H., Kleimann, J., & Kissmann, R. 2015, *ApJ*, 805, 155
- Wiengarten, T., Oughton, S., Engelbrecht, N. E., et al. 2016, *ApJ*, 833, 17
- Zank, G. P., Adhikari, L., Hunana, P., et al. 2017, *ApJ*, 835, 147
- Zank, G. P., Dosch, A., Hunana, P., et al. 2012, *ApJ*, 745, 35
- Zank, G. P., Li, G., Florinski, V., et al. 2004, *Journal of Geophysical Research (Space Physics)*, 109, A04107
- Zank, G. P., & Matthaeus, W. H. 1992, *J. Geophys. Res.*, 97, 17
- Zank, G. P., & Matthaeus, W. H. 1993, *Physics of Fluids A*, 5, 257
- Zank, G. P., Matthaeus, W. H., Bieber, J. W., & Moraal, H. 1998, *J. Geophys. Res.*, 103, 2085
- Zank, G. P., Matthaeus, W. H., & Smith, C. W. 1996, *J. Geophys. Res.*, 101, 17093
- Zhang, M. 1997, *ApJ*, 488, 841
- Zhang, M. 1999, *ApJ*, 513, 409
- Zhang, M., Luo, X., & Pogorelov, N. 2015, *Physics of Plasmas*, 22, 091501
- Zhao, L.-L., Adhikari, L., Zank, G. P., Hu, Q., & Feng, X. S. 2017, *ApJ*, 849, 88
- Zhao, L.-L., Qin, G., Zhang, M., & Heber, B. 2014, *Journal of Geophysical Research (Space Physics)*, 119, 1493
- Zhao, L.-L., & Zhang, H. 2015, *ApJ*, 805, 6
- Zhao, L.-L., & Zhang, H. 2016, *ApJ*, 827, 13
- Zhou, Y., & Matthaeus, W. H. 1990, *J. Geophys. Res.*, 95, 10291
- Zurbuchen, T. H. 2007, *ARA&A*, 45, 297
- Zurbuchen, T. H., Schwadron, N. A., & Fisk, L. A. 1997, *J. Geophys. Res.*, 102, 24175

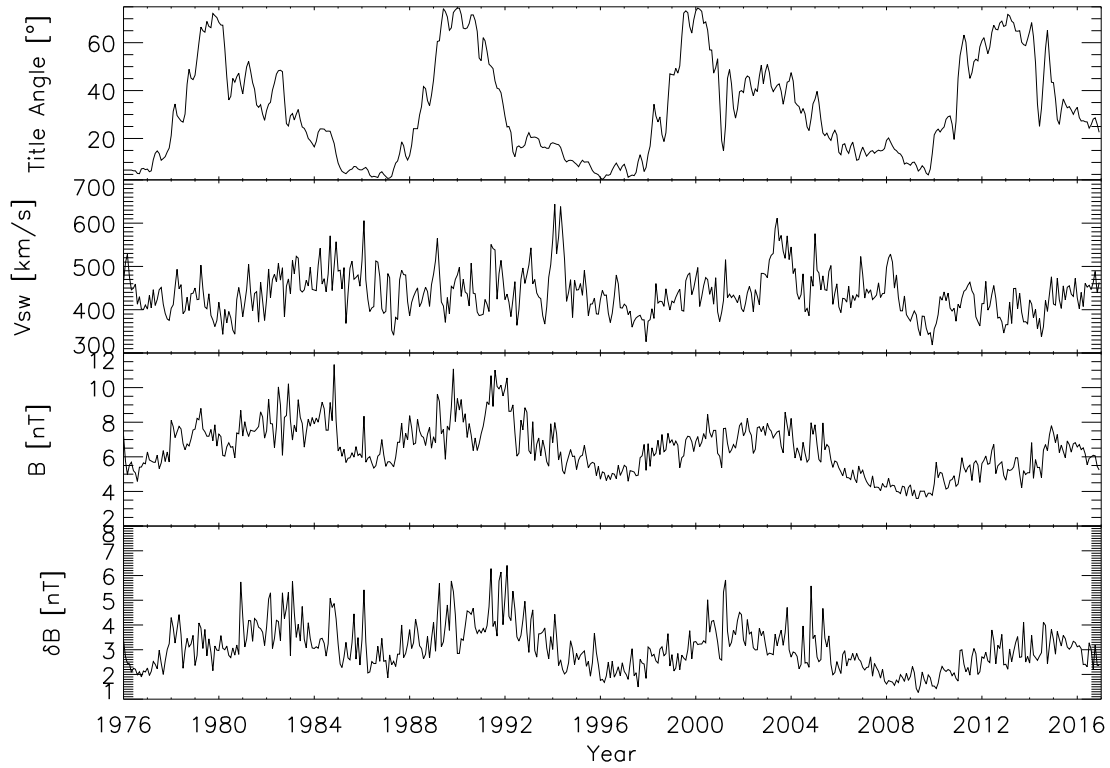


**Figure 1.** Interplanetary parameters at 1 au. Top panel shows the tilt angle of heliospheric current sheet from the WSO website ([wso.stanford.edu](http://wso.stanford.edu)) with the “new” model. Second and third panels represent averaged solar wind velocity and averaged magnetic field strength for each month, respectively. Black line in the bottom panel means the magnetic turbulence magnitude calculated using method described in Qin & Shen (2017), and minutely HMF data from OMNI website ([omniweb.gsfc.nasa.gov](http://omniweb.gsfc.nasa.gov)) is used to get more accurate result.

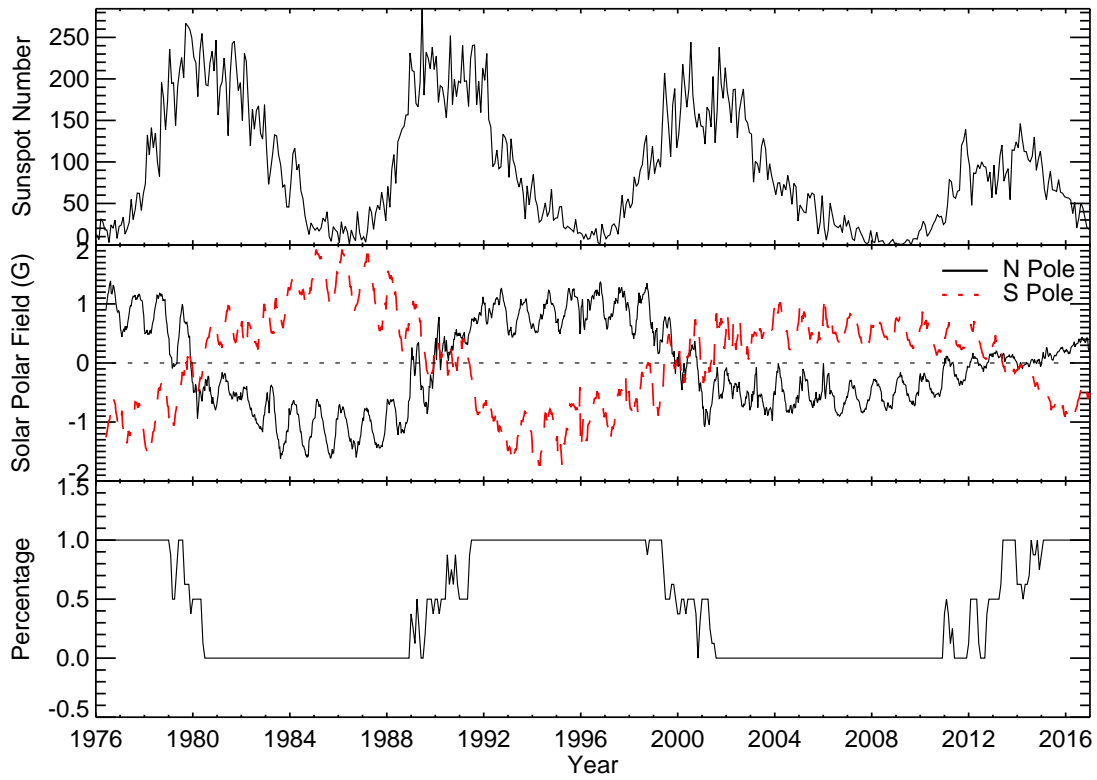


**Figure 2.** Top panel shows the monthly sunspot number from WDC-SILSO ([sidc.oma.be](http://sidc.oma.be)). The second panel means the north (black line) and south (red dashed line) solar polar field from WSO ([wso.stanford.edu](http://wso.stanford.edu)). Bottom panel represents the possibility of  $A > 0$  for each month. See the text for more details.

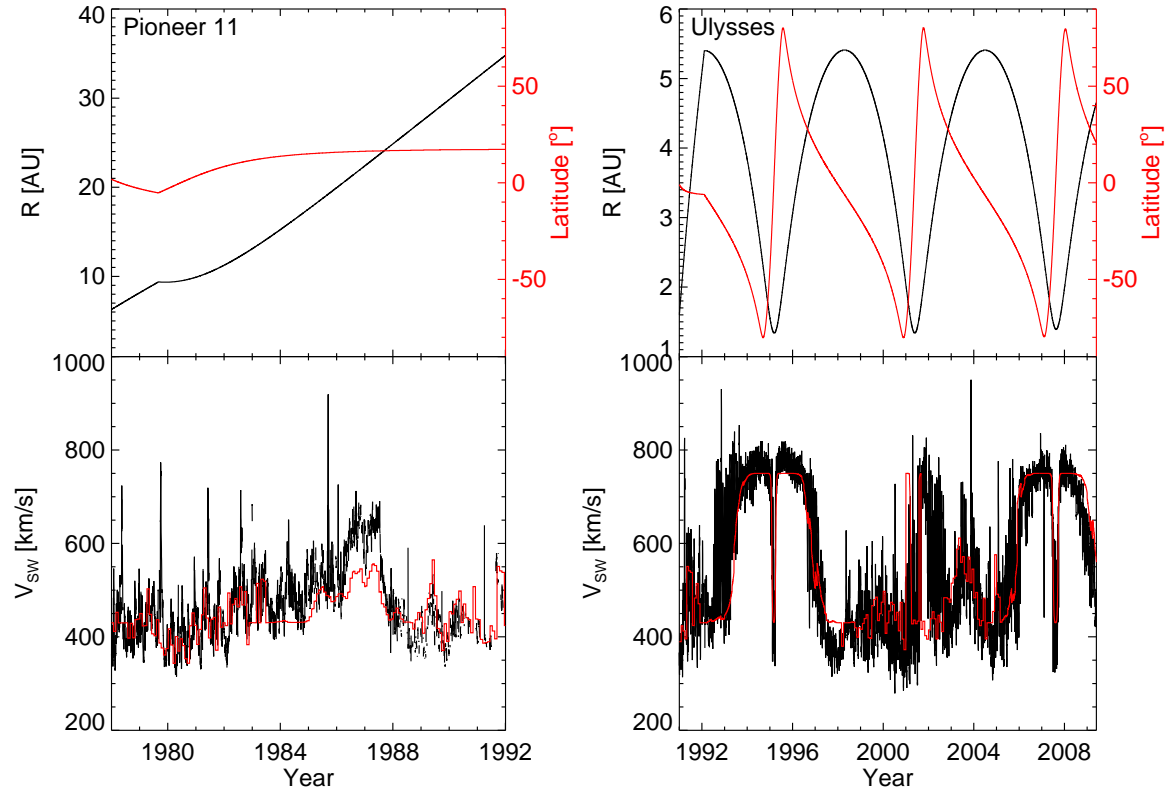


**Figure 3.** Left: Top panel shows the radial distance (black line) and heliographic latitude (red line) of Pioneer 11. Bottom panel means the comparison between the results of Equation (6) (red line) along the trajectory of Pioneer 11 and the daily solar wind speed observed by Pioneer 11 (black line). Right: The same to Figure 3 (left) except that for Ulysses.

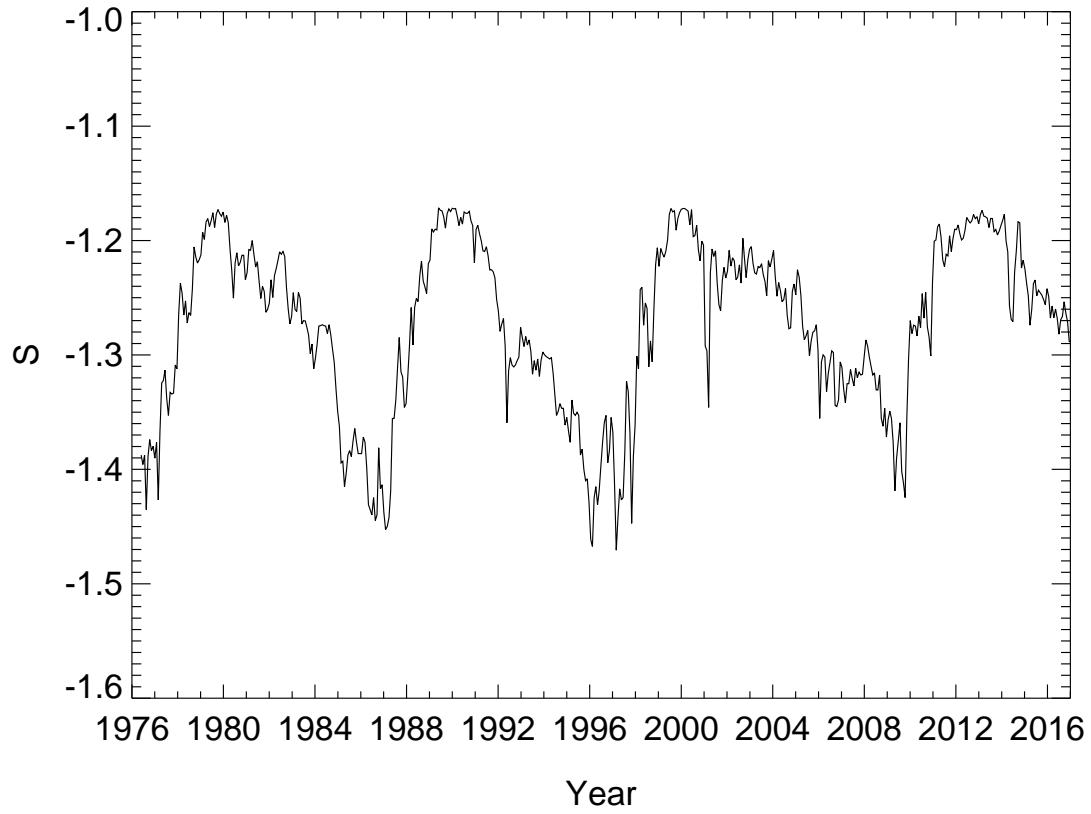


**Figure 4.**  $S$  in Equation 17 varies with solar cycles.

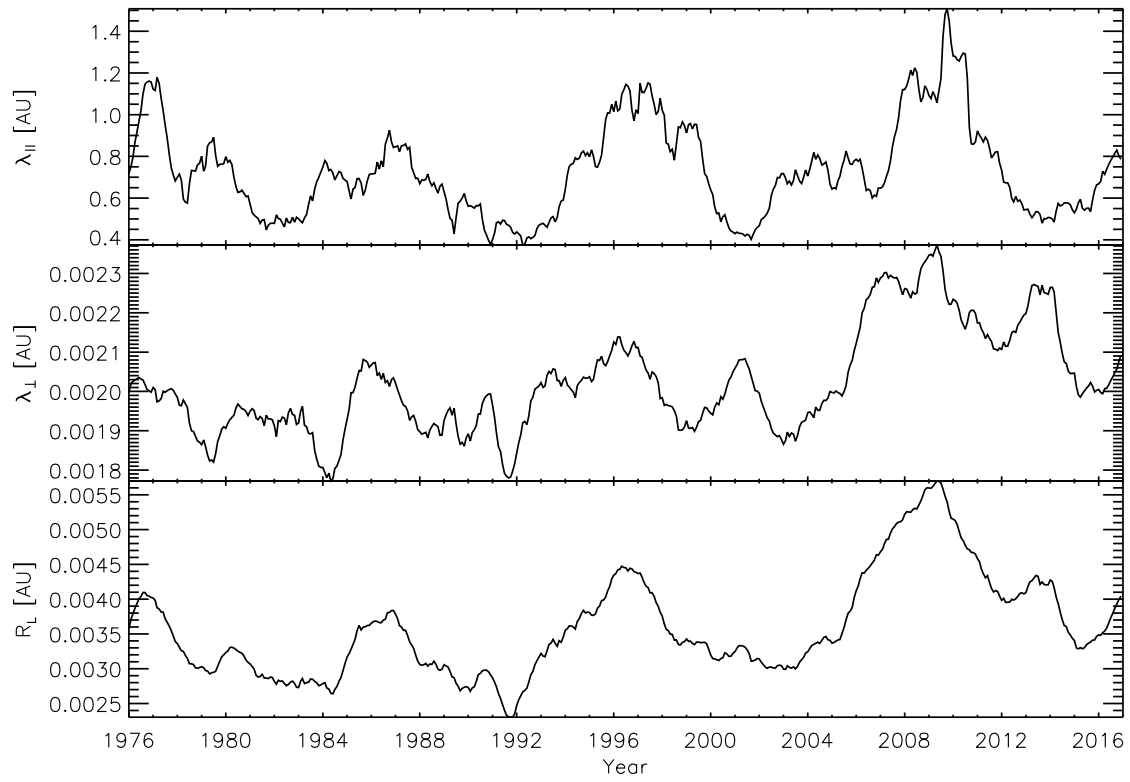


**Figure 5.** Computed monthly parallel and perpendicular mean-free paths as well as the particle's gyro-radius for 1 GV proton near Earth. The 13-month smoothed results are presented in this figure as the original values show too many spikes.

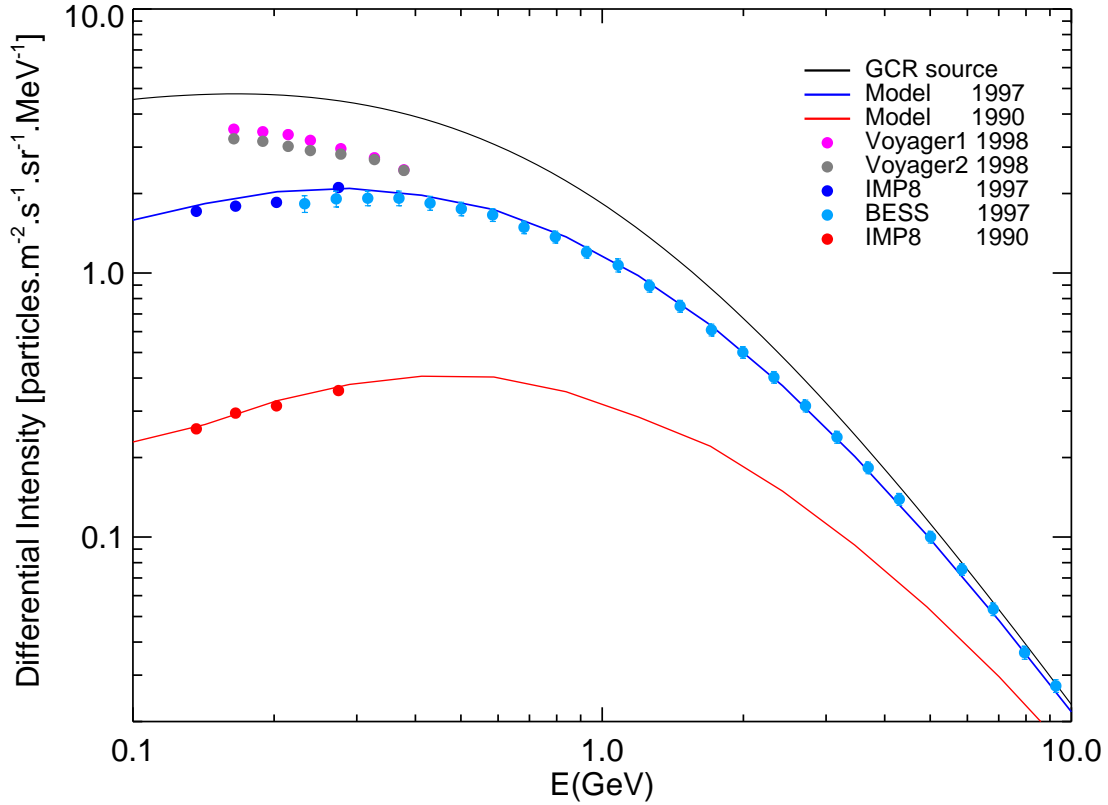


**Figure 6.** Computed GCR proton energy spectra at Earth near solar minimum in 1997 (blue line) and near solar maximum in 1990 (red line), as well as observations of various instruments. The black line means GCR source used in this work (Qin & Shen 2017). Magenta and gray solid circles denote Voyager 1 and Voyager 2 observations in 1998 reported by Webber et al. (2006). Blue and sky blue solid circles represent IMP 8 data in 1997 from Webber & Higbie (2003) and data from the BESS magnetic spectrometer in 1997 (Shikaze et al. 2007). Red solid circles refer to yearly averaged GCR proton flux, which has been processed to get the GCR background using the despiking algorithm (Qin et al. 2012), from IMP 8 in 1990.

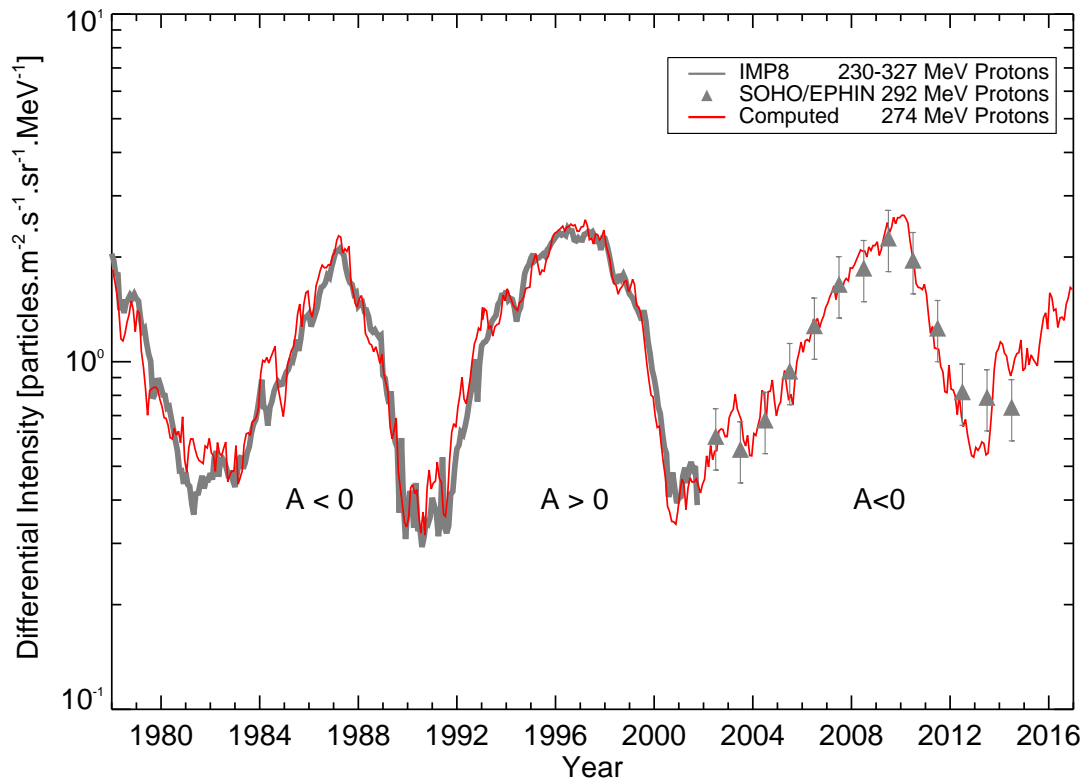


**Figure 7.** Comparison between the computed monthly 274 MeV proton intensity at Earth (red line) with observations of spacecraft from 1978 to 2016. The gray line means monthly averaged GCR proton intensity, which has been processed to get the GCR background using the despiking algorithm (Qin et al. 2012), from IMP 8 observations with energy range in 230 – 327 MeV. Gray triangles represent yearly 292 MeV proton flux observed by SOHO/EPHIN (Kühl et al. 2016).

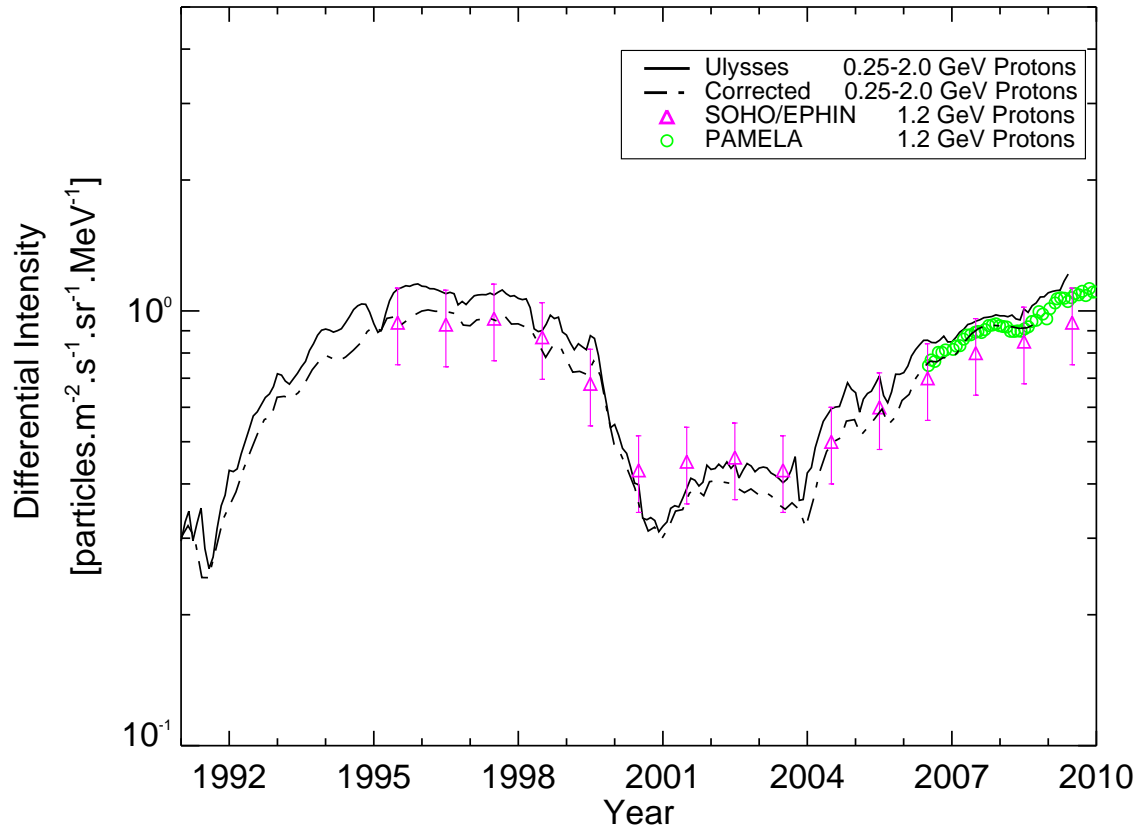


**Figure 8.** Monthly averaged 0.25 – 2.0 GeV proton flux data observed by KET onboard Ulysses is shown as black solid line. The proton intensity data for this channel, which are originally obtained as daily count rates from the Ulysses Final Archive ([ufa.esac.esa.int/ufa](http://ufa.esac.esa.int/ufa)), are divided by the corresponding response factor to get the proton flux. The dashed-dotted line means the 1 au equivalent 0.25 – 2.0 GeV proton flux, and the relevant count rates are digitized from Figure 5 in Heber et al. (2009). Note that the raw count rates are corrected by the spatial variations of Ulysses with the spatial gradients of GCR proton intensity (Heber et al. 2009) to get the 1 au equivalent count rates. In addition, the 1.2 GeV proton flux observed by SOHO/EPHIN (Kühl et al. 2016) and PAMELA (Adriani et al. 2013) are shown as magenta triangles and green circles, respectively.

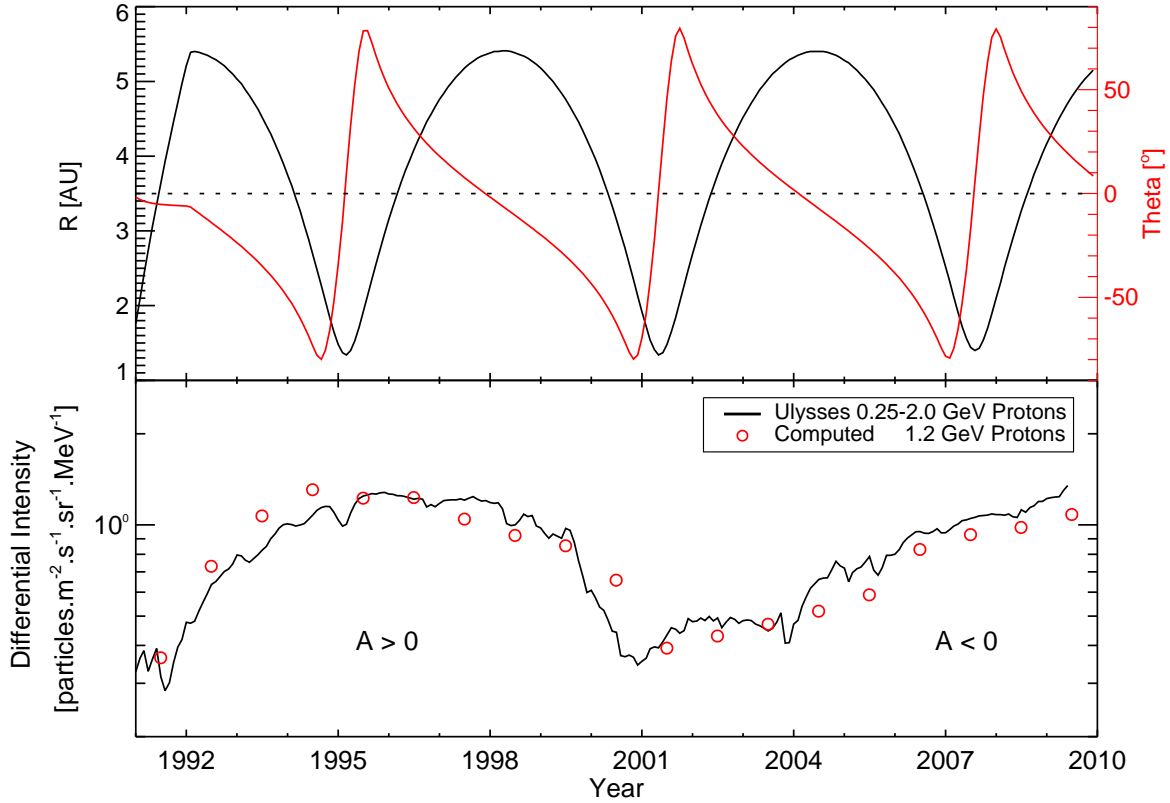


**Figure 9.** Top panel shows the radial distance (black line) and heliographic latitude (red line) of Ulysses. Computed yearly 1.2 GeV proton intensity along the Ulysses trajectory science 1991 (red circles) and monthly averaged proton intensity observations with energy range in 0.25 – 2.0 GeV (black line) from 1991 to 2009 are illustrated in the bottom panel.

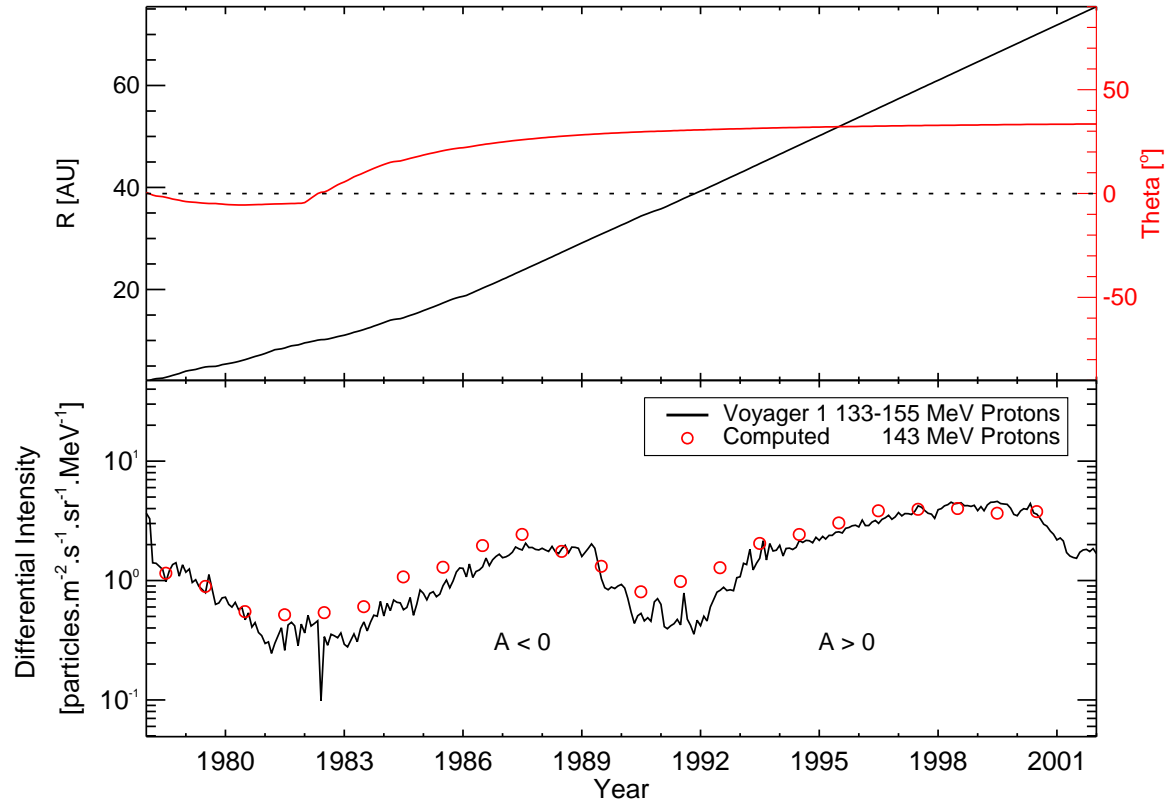


**Figure 10.** Top panel shows the radial distance (black line) and heliographic latitude (red line) of Voyager 1. Computed yearly 143 MeV proton intensity along the Voyager 1 trajectory science 1978 (red circles) and monthly averaged proton intensity observations with energy range in 133 – 155 MeV (black line) from 1978 to 2000 are illustrated in the bottom panel.

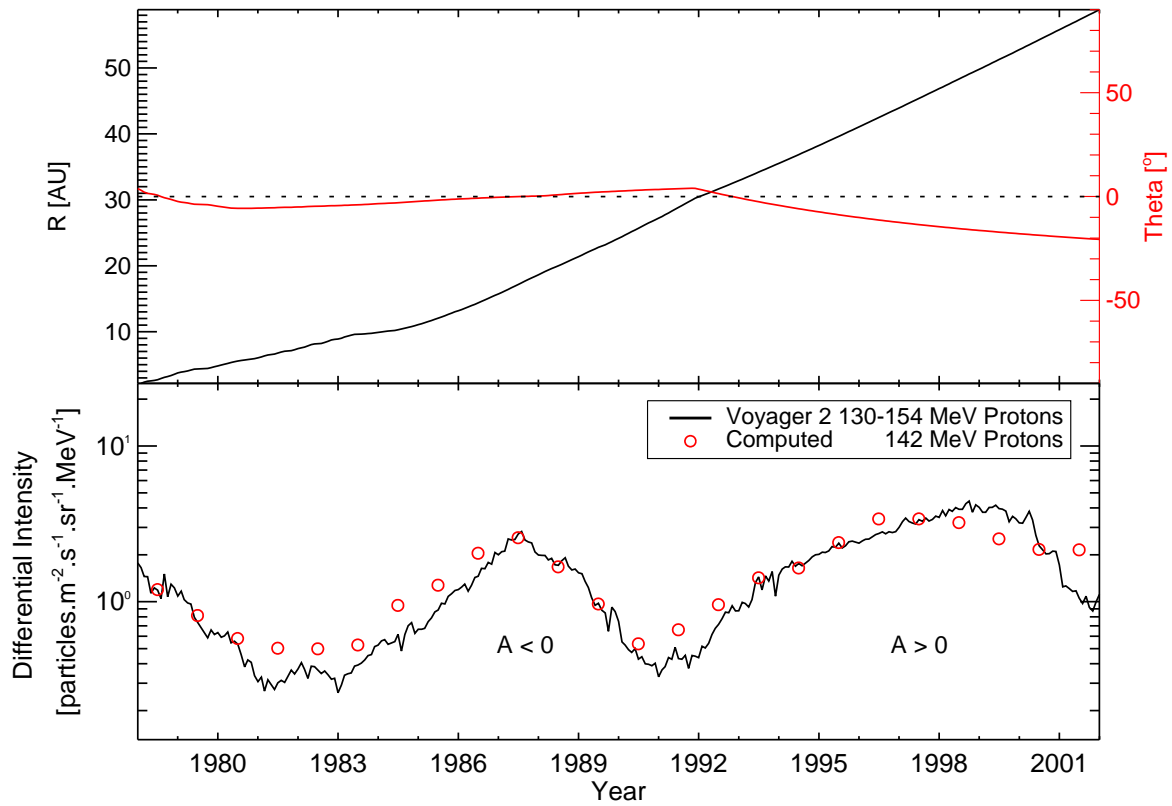


**Figure 11.** Top panel shows the radial distance (black line) and heliographic latitude (red line) of Voyager 2. Computed yearly 142 MeV proton intensity along the Voyager 2 trajectory science 1978 (red circles) and monthly averaged proton intensity observations with energy range in 130 – 154 MeV (black line) from 1978 to 2001 are illustrated in the bottom panel.